

Radial velocity variability and stellar properties of FGK stars in the cores of NGC 2516 and NGC 2422

John I. Bailey, III,¹^{*} Mario Mateo,² Russel J. White,³ Stephen A. Sackett⁴ and Jeffrey D. Crane⁴

¹*Leiden Observatory, Leiden University, PO Box 9513, NL-2300RA Leiden, The Netherlands*

²*Department of Astronomy, University of Michigan, 1085 South University, Ann Arbor, MI 48109, USA*

³*Department of Physics, and Astronomy, Georgia State University, PO Box 4106, Atlanta, GA 30302, USA*

⁴*Carnegie Observatories, 813 Santa Barbara Street, Pasadena, CA 91101, USA*

Accepted 2017 December 13. Received 2017 December 13; in original form 2016 September 12

ABSTRACT

We present multi-epoch high-dispersion optical spectra obtained with the Michigan/Magellan Fibre System of 126 and 125 Sun-like stars in the young clusters NGC 2516 (141 Myr) and NGC 2422 (73 Myr). We determine stellar properties including radial velocity (RV), T_{eff} , $[\text{Fe}/\text{H}]$, $[\alpha/\text{Fe}]$ and the line-of-sight rotation rate, $v_r \sin(i)$, from these spectra. Our median RV precision of 80 m s^{-1} on individual epochs that span a temporal baseline of 1.1 yr enables us to investigate membership and stellar binarity, and to search for sub-stellar companions. We determine membership probabilities and RV variability probabilities for our sample along with candidate companion orbital periods for a select subset of stars. In NGC 2516, we identified 81 RV members, 27 spectroscopic binaries (17 previously identified as photometric binaries) and 16 other stars that show significant RV variability after accounting for average stellar jitter at the 74 m s^{-1} level. In NGC 2422, we identify 57 members, 11 spectroscopic binaries and three other stars that show significant RV variability after accounting for an average jitter of 138 m s^{-1} . We use Monte Carlo simulations to verify our stellar jitter measurements, determine the proportion of exoplanets and stellar companions to which we are sensitive, and estimate companion-mass limits for our targets. We also report mean cluster metallicity, velocity and velocity dispersion based on our member targets. We identify 58 non-member stars as RV variables, 24 of which have RV amplitudes that imply stellar or brown-dwarf mass companions. Finally, we note the discovery of a separate RV clustering of stars in our NGC 2422 sample.

Key words: techniques: radial velocities – techniques: spectroscopic – planets and satellites: detection – stars: abundances – binaries: spectroscopic – open clusters and associations: individual: (NGC 2516, NGC 2422).

1 INTRODUCTION

Exoplanets found in open stellar clusters have significant potential to inform our understanding of planetary formation and system evolution (e.g. Paulson, Cochran & Hatzes 2004; Quinn et al. 2012, 2014; Meibom et al. 2013; Howell et al. 2014; Brucalassi et al. 2014; Bailey et al. 2016). Their appeal stems from the well-known ages and well-characterized environments offered by open clusters. This allows planets found therein generally to offer greater leverage on the relative importance that core accretion (Mizuno et al. 1980) and disc gravitational instabilities (Boss 1997) play in formation and the various migration mechanisms play in the evolution

of so-called hot Jupiters (e.g. disc coupling, Goldreich & Tremaine 1980; Lin, Bodenheimer & Richardson 1996; dynamical scattering, Rasio & Ford 1996; Jurić & Tremaine 2008; or even secular interactions, Fabrycky & Tremaine 2007). Unfortunately, the number of exoplanets confirmed at present in clusters remains small (< 10), despite the considerable effort expended in finding such systems. This reflects the difficulty of surveying large numbers of stars in clusters to sufficiently high velocity precision suitable for the detection of exoplanets.

In Bailey et al. (2016, hereafter B16), we introduced a new approach to obtain highly multiplexed radial velocities (RVs) with sufficient precision to detect warm and hot Jupiters around solar analogues in open cluster out to ~ 1 kpc using the Michigan/Magellan Fibre System (M2FS; Mateo et al. 2012). We showed that we are able to measure RVs for up to 128 stars over a half-degree

* E-mail: baileyji@umich.edu

Table 1. Pointings.

Cluster	Messier	RA (2000)	Dec. (2000)	Age (Myr)	Distance (pc)	$E(B - V)$	N_{epoch}	N_{targ}	V	$B - V$
NGC 2516	–	7:58:42	–60:46:36	141	346	0.11	12	126	11.68–15.09	0.46–1.26
NGC 2422	M47	7:36:30	–14:29:42	73	491	0.07	10	125	12.20–16.10	0.45–1.43

Note. The coordinates listed correspond to our field centres and, although near, are not at the cluster centre. Both distances as well as the reddening for NGC 2422 are from Kharchenko et al. (2005). Target photometry is from J01 (NGC 2516) and P03/UCAC4 (NGC 2422). The reddening for NGC 2516 is from Sung et al. (2002). The age for NGC 2516 is from Meynet, Mermilliod & Maeder (1993) and for NGC 2422 from Loktin, Gerasimenko & Malysheva (2001). Note that Kharchenko et al. (2005) gives ages of 120 and 132 Myr, albeit with errors of ~ 70 Myr.

field of view with a measurement precision of 25 m s^{-1} for sufficiently bright, slowly rotating ($\lesssim 10 \text{ km s}^{-1}$), Sun-like stars and to $45\text{--}65 \text{ m s}^{-1}$ at magnitudes typical for such stars in open clusters within 1 kpc. We also showed that we are able to obtain precise measurements of T_{eff} , [Fe/H], $[\alpha/\text{Fe}]$ and $v_r \sin(i)$. Our technique, thus, allows us to search efficiently for warm and hot Jupiters in open clusters with ages ranging from about 100 Myr to nearly 1 Gyr while simultaneously characterizing their host environment well.

As a first test of our technique, we carried out a survey of all the Sun-like stars in the cores of the 141-Myr-old open cluster NGC 2516 and 73-Myr-old cluster NGC 2422, the youngest open clusters yet surveyed using RV techniques. Here we report the first results of our survey: effective temperatures (T_{eff}), iron and light element abundances ([Fe/H] and $[\alpha/\text{Fe}]$ from template fitting), projected rotational velocity [$v_r \sin(i)$], mean radial velocity ($\overline{\text{RV}}$) and observed RV standard deviation (σ_{obs}) measurements for the 251 stars in our sample, 126 in NGC 2516 and 125 in NGC 2422. We also report RV-based membership probabilities and cluster properties (e.g. velocity dispersion, binary fraction and abundance) and examine the level of stellar jitter in each cluster. Finally, we identify all stars in our sample that exhibit statistically significant RV variability, reporting a number of spectroscopic binaries and identifying a small number of potential exoplanet hosts that merit further investigation.

In Section 2, we review our observational programme and the details of the specific stars we target in NGC 2516 and NGC 2422. Then, in Section 3, we review our analysis methodology and present stellar properties for our targets. Section 4 describes our approach to spectroscopic binaries in our sample and the Monte Carlo simulations we used to investigate a number of questions related to binarity, membership and stellar jitter later in this text. We use Section 5 to detail our RV membership approach, describe a small number of notable stars, report our findings for both NGC 2516 and NGC 2422, and also note the presence of a separate association of stars contaminating our NGC 2422 sample. Section 6 looks at the cluster RV, RV dispersion and the projected rotation and metallicity of cluster members. Here we consider the RV dispersion, binary fraction and abundances of both clusters. We also compare the cluster $v_r \sin(i)$ distributions with that of the Pleiades. In Section 7, we investigate the level of stellar jitter in our targets and determine an average level for each cluster. Finally, Section 8 presents the results of our RV variability analysis. We cover our companion-mass limits and report a number of RV variables – including several with significant periodicities indicative of stellar or sub-stellar companions meriting a prompt follow-up.

2 STELLAR SAMPLE AND OBSERVATIONS

We selected Sun-like stars in the 141-Myr- and 73-Myr-old open clusters NGC 2516 and NGC 2422 as targets for our study. These clusters are within 500 pc. They are rich in solar analogues and

have approximately solar metallicity. They both have recent photometric membership catalogues that are photometrically complete for selecting Sun-like targets (Jeffries, Thurston & Hambly 2001; Prisinzano et al. 2003, hereafter J01 and P03), and they have angular sizes and sky densities that are well matched to the 128 fibres M2FS can deploy across its half-degree field of view. Table 1 – from B16 – provides the coordinates, colour and magnitude ranges, and number of epochs obtained for our pointings in each cluster along with cluster age, distance and reddening.

In NGC 2516, we selected targets that J01 identified as photometric single (79) or binary (47) members with colours and magnitudes consistent with F5V–K5V spectral types in our field of view, which was also constrained by our need for a bright central star for use as a Shack–Hartman reference. This sample of 126 stars was then cross-matched with the UCAC4 catalogue (Zacharias et al. 2013) to extract astrometry. In NGC 2422, we used the same approach to select photometric members (100) from the P03 catalogue, which does not distinguish between single and binary members. Due to the smaller number of P03 targets, we expanded our selection out in colour from the MS defined by P03 members using the UCAC4 catalogue until we had sufficient targets to fill the available fibres, selecting an additional 25 stars in our adopted pointing. We stress that with the available fibres, we are able to target every star in each half-degree field that could plausibly be a solar-analogue member.

We refer to the total sample of 126 stars in NGC 2516 and the 100 stars from P03 in NGC 2422 as photometric members in this paper and the additional 25 targets in NGC 2422 as candidate members. The photometric properties and positions of both the parent samples and final observed samples are illustrated in Figs 1 and 2, which show colour–magnitude diagrams and sky charts for NGC 2516 and NGC 2422. Tables A1 and A2, provided only as machine-readable tables online and at the CDS, list target IDs, coordinates, literature photometry, number of usable epochs (signal to noise $S/N > 12$) and the mean per-pixel S/N for each target. They also report numerous other results that will be described in later sections. Table 2 lists the contents of these tables and provides references to the pertinent sections of the text while Table 3 provides an abbreviated example of Table A1.

As described in B16, we also targeted six stars with similar RAs from the *Gaia* RVS catalogue (Soubiran et al. 2013) for use as RV standards and to test our stellar property analysis. A summary of these stars is given in table 3 of B16.

We observed our targets using M2FS, a multi-object fibre-fed spectrograph located on the Magellan/Clay 6.5-m telescope at Las Campanas Observatory in Chile. M2FS was employed in cross-dispersed echelle mode with $45\text{-}\mu\text{m}$ fibre slits and the Hot Jupiter filter to obtain $\sim 130\text{-}\text{\AA}$ -wide spectra centred at 7230\AA with a median resolving power of 50 000 (R varies slightly with fibre, wavelength and focus) and a median per-pixel S/N of 50 for all 251 of our targets. This wavelength region was selected for its optimal combination of telluric and stellar absorption lines, the former of

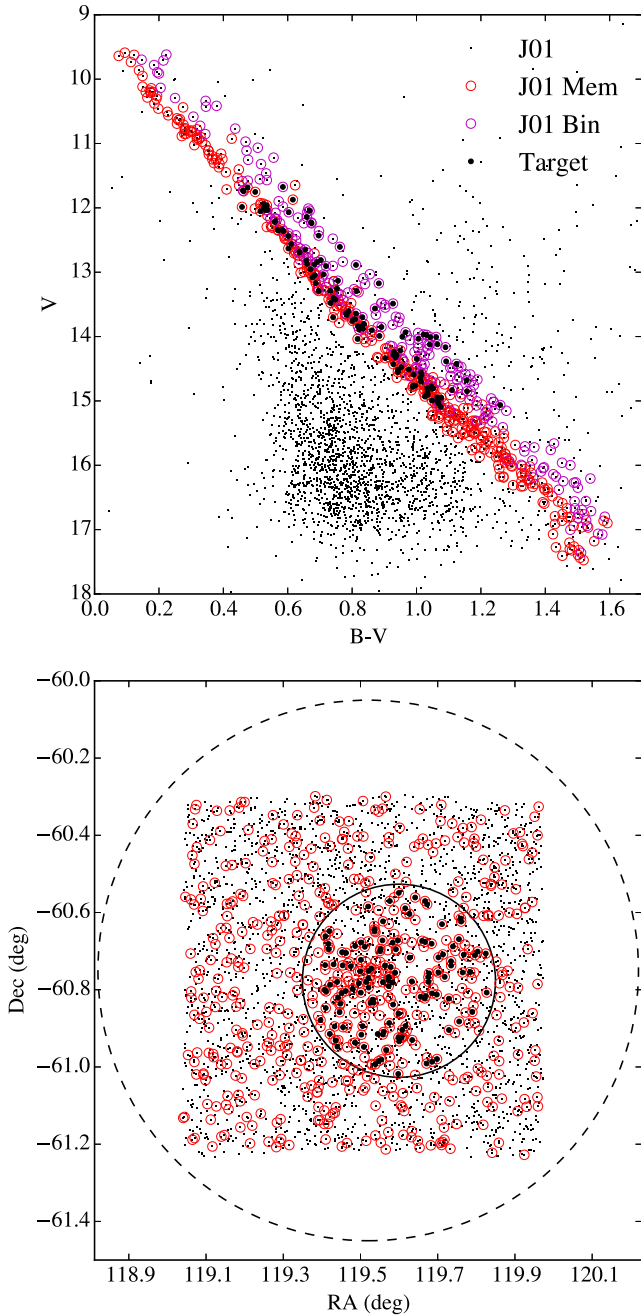


Figure 1. Colour–magnitude diagram and sky plot of our pointing in NGC 2516. Upper: Stars in the **J01** catalogue as minuscule black points with stars flagged as photometric single members circled in red or photometric member binaries in purple. Stars we targeted are shown as large black marks. Lower: NGC 2516 stars with all photometric members (single or binary) circled in red. The square is the CCD footprint used by **J01**. The dashed black circle represents the cluster’s nominal radius as reported in Kharchenko et al. (2005) and the solid black circle the M2FS field of view around our pointing centre.

which our modelling process uses as a simultaneous measure of both the wavelength-to-pixel mapping and the instrument point-spread function. Further details of the M2FS configuration we used, our rationale for this wavelength region and data reduction procedure are provided in B16.

The dates, number of stars targeted, median per-pixel S/N and total exposure times (typically from three or four back-to-back ex-

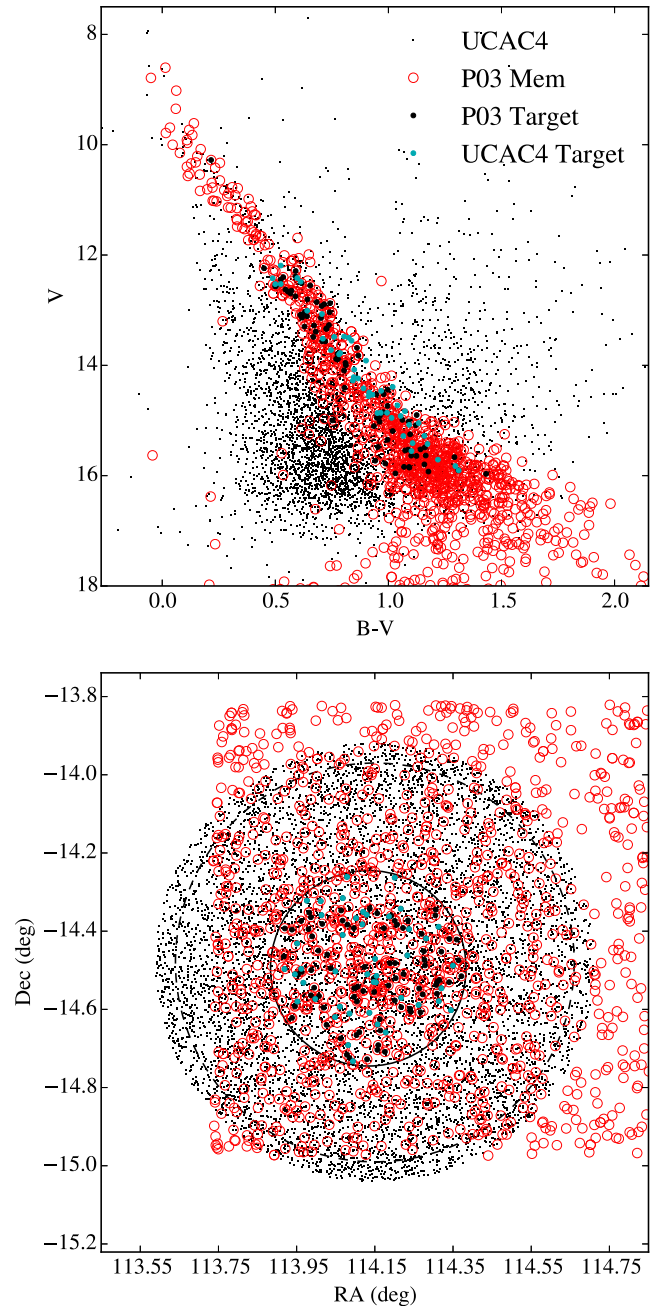


Figure 2. Colour–magnitude diagram and sky plot of our pointings in NGC 2422. Upper: Stars in the UCAC4 catalogue within 1.1 cluster radii of the centre of NGC 2422. Stars in the **P03** catalogue (which includes only photometric members) are circled in red. Our targets are shown as large black marks if from **P03** or cyan marks if from UCAC4. Lower: NGC 2422 stars with photometric members circled in red. The square is the CCD footprint used by **P03**. The dashed black circle represents the cluster’s nominal radius as reported in Kharchenko et al. (2005) and the solid black circle the M2FS field of view around our pointing centre.

posures) for each of our epochs are listed in Table 4. Exposure times ranged from 1.7 h to 3.1 h and median per-pixel S/N from 28 to 65. In two epochs, operational issues resulted in eight and 23 stars not being targeted. Over the course of our campaign, an evolving set of damaged or dead fibres impacted our ability to obtain spectra of various targets. This, along with a wide magnitude range and variable seeing, resulted in a number of targets for which some (in

Table 2. Columns in online Tables A1 (NGC 2516) and A2 (NGC 2422).

Column	Name	Unit	Description
1	ID	–	UCAC4 ID
2	LitID	–	J01 (NGC 2516) or P03 (NGC 2422) ID (if extant)
3	RAdeg	deg	Right ascension from UCAC4
4	DEdeg	deg	Declination from UCAC4
5	Vmag	mag	<i>V</i> magnitude
6	B-V	mag	<i>B</i> – <i>V</i> colour
7	PSrc	–	Photometry source: J01 (NGC 2516), P03 (NGC 2422) or U (UCAC4)
8	N	–	Number of usable spectra obtained
9	S/N	–	Mean S/N (per pixel)
10	Teff	K	Adopted effective temperature, including correction for members (Section 3.2)
11	e+_Teff	K	Upper 1 σ uncertainty on T_{eff}
12	e-_Teff	K	Lower 1 σ uncertainty on T_{eff}
13	f_Teff	–	[0,1] T_{eff} correction applied
14	[Fe/H]	dex	Adopted [Fe/H] abundance (Section 3.2)
15	e+_ [Fe/H]	dex	Upper 1 σ uncertainty on [Fe/H]
16	e-_ [Fe/H]	dex	Lower 1 σ uncertainty on [Fe/H]
17	[α /Fe]	dex	Adopted α -element abundance (Section 3.2)
18	e+_ [α /Fe]	dex	Upper 1 σ uncertainty on [α /Fe]
19	e-_ [α /Fe]	dex	Lower 1 σ uncertainty on [α /Fe]
20	vrot	km s ⁻¹	Adopted line-of-sight stellar rotational velocity (Section 3.2)
21	e+_vrot	km s ⁻¹	Upper 1 σ uncertainty on $v_r \sin(i)$
22	e-_vrot	km s ⁻¹	Lower 1 σ uncertainty on $v_r \sin(i)$
23	log(<i>g</i>)	–	log(<i>g</i>) adopted for fitting (Section 3.2)
24	RVel	m s ⁻¹	Weighted mean barycentric RV (Section 3.2)
25	e_RVel	m s ⁻¹	Bootstrapped error on the weighted mean barycentric RV
26	sig_obs	m s ⁻¹	σ_{obs} , error weighted standard deviation of measured RVs (Section 3.2)
27	sig_meas	m s ⁻¹	σ_{meas} , mean RV measurement error (Section 3.2)
28	Pmem	–	P_{RV} , RV membership probability (Section 5)
29	Mem	–	Membership flag: member (M), non-member (N), probable member (P), no-data (X) (Section 5)
30	Type	–	RV single (S), RV binary (B), double-lined binary (SB2), continuum (C), no-data (X) (Section 4, Section 5.1)
31	sig_jit	m s ⁻¹	Adopted stellar jitter, σ_{jitter} (Section 7)
32	Pvar	–	Probability that target is an RV variable (Section 8)
33	Pvar_jit	–	Probability that target is an RV variable in the presence of adopted stellar jitter (Section 8)
34	Period	days	Optimized value of most significant periodogram peak above 95 per cent confidence interval (Section 8.1)
35	M3	M_{Jup}	95 per cent companion-mass limit at 3 d (Section 8.2)
36	M10	M_{Jup}	95 per cent companion-mass limit at 10 d (Section 8.2)
37	M20	M_{Jup}	95 per cent companion-mass limit at 20 d (Section 8.2)
38	Mstar	M_{\odot}	Stellar mass adopted for companion detectability test (Section 8.2)

Table 3. Example of online Table A1: Properties of targets in NGC 2516.

ID	Literature ID	RA (deg)	Dec. (deg)	<i>V</i> (mag)	<i>B</i> – <i>V</i> (mag)	PSrc	<i>N</i>	$\overline{S/N}$	T_{eff} (K)	$f_{T_{\text{eff}}}$	[Fe/H] (dex)	[α /Fe] (dex)	$v_r \sin(i)$ (km s ⁻¹)	log(<i>g</i>)
147-012265	7864	119.50997	–60.77981	12.07	0.603	J01	11	115	6447 ± 50	1	–0.25 ± 0.04	0.04 ^{+0.01} _{–0.02}	16.9 ± 0.5	4.4
147-012424	11307	119.89213	–60.71620	13.70	0.741	J01	12	54	6116 ⁺³⁵ _{–33}	1	–0.09 ± 0.02	0.03 ^{+0.01} _{–0.02}	6.4 ± 0.2	4.5
146-012601	11233	119.88376	–60.81251	13.88	0.834	J01	10	39	5239 ± 19	1	–0.29 ± 0.02	0.12 ± 0.01	16.1 ± 0.2	4.6
147-012249	7590	119.48121	–60.72243	13.99	0.885	J01	12	51	5372 ⁺¹⁷ _{–13}	1	–0.14 ± 0.01	0.06 ± 0.01	6.7 ± 0.1	4.6
147-012499	12874	120.08582	–60.71043	13.49	0.927	J01	12	51	5480 ± 79	1	–0.36 ± 0.10	0.06 ± 0.01	8.4 ± 1.3	4.5
RV (m s ⁻¹)	σ_{obs} (m s ⁻¹)	σ_{meas} (m s ⁻¹)	P_{mem}	Mem.	Type	σ_{jit} (m s ⁻¹)	P_{var}	$P_{\text{var, jit}}$	Period (day)	M_3 (M_{Jup})	M_{10} (M_{Jup})	M_{20} (M_{Jup})	M_{star} (M_{\odot})	
37 677 ± 11 052	35 789	196	0.00	P	SB2	74	1.00	1.00	–	7.9	12.2	23.9	1.17	
15 450 ± 6734	23 160	75	0.00	P	SB2	74	1.00	1.00	30.0	3.7	5.6	11.3	1.11	
31 158 ± 6325	19 304	159	0.00	P	B	74	1.00	1.00	1.9	5.8	9.0	21.8	0.82	
25 997 ± 4535	16 386	62	0.86	M	B	74	1.00	1.00	23.2	3.0	4.5	9.2	0.89	
18 343 ± 4125	14 814	87	0.00	P	SB2	74	1.00	1.00	78.7	3.5	5.4	10.8	0.87	

Note. Tables A1 and A2 are available online in machine-readable format. Table 2 provides a description of the columns in the full table.

Table 4. Cluster observations.

Date	N	Median S/N	Exposure time (s)
NGC 2516			
2013 November 22	118	57	6600
2013 November 24	126	28	6000
2013 November 27	126	38	6300
2013 November 28	126	59	7200
2013 November 30	126	44	6800
2014 February 16	103	46	9600
2014 February 17	126	65	9000
2014 February 21	126	57	9000
2014 December 9	126	48	7200
2014 December 10	126	33	7200
2014 December 11	126	63	9000
2014 December 12	126	55	7200
NGC 2422			
2013 December 1	125	60	7200
2014 February 18	125	55	9000
2014 February 19	124	46	7200
2014 February 22	124	41	7200
2014 February 26	125	38	9000
2014 December 12	125	35	9000
2014 December 13	125	51	10150
2014 December 17	125	71	9800
2014 December 20	125	57	11200
2014 December 22	125	59	10800

one case, all) of our spectra fell below the S/N limit (12) at which we are able to run our analysis reliably (see Section 3).

3 SPECTROSCOPICALLY MEASURED STELLAR PROPERTIES

3.1 Analysis

Here we review the key methods and performance of our analysis procedure. Full details can be found in B16. The exposures obtained with M2FS were individually bias-corrected and treated with the L.A. Cosmic algorithm (van Dokkum 2001) to detect and flag cosmic ray hits. We did not flat-field our data due to limitations in the M2FS flat-field system. Frames were then summed, correcting for both cosmic ray hits and scattered light. The spectra in each frame were traced and extracted to 1D using PyRAF APALL. Throughout this process, we maintained a variance frame and performed an identical extraction on it to obtain a variance spectrum, which we use for determining the mean per-pixel S/N and in the fitting process to weight each pixel.

We fitted a model of each spectrum built from a telluric transmission template (Wallace et al. 2011) and a synthetic spectrum interpolated from the PHOENIX grid (Husser et al. 2013) to each of our spectra and adopted the mean of the best-fitting values of T_{eff} , $[\text{Fe}/\text{H}]$, $[\alpha/\text{Fe}]$ and $v_r \sin(i)$ as our values for each star. When fitting, we use

$$\log(g) = \log \left(\frac{9.44 \times 10^9}{(T_{\text{eff}}/\text{K})^{16/11}} \right), \quad (1)$$

which is derived from the mass–luminosity, mass–radius and temperature–luminosity relations, to compute values for $\log(g)$ that are sufficiently accurate. The resulting $\log(g)$ values are likely representative of the true values for member stars in NGC 2516 and NGC 2422. We caution that the values we report are not

measurements of $\log(g)$ and stress that our results are not appreciably affected by the sub half-dex error this approximation may cause. Additional details and the derivation of equation (1) are in section 4.1.1 of B16.

RVs were determined in a final iteration of fits in which stellar properties are held fixed at their adopted values as described above. The exact iterative process was determined by optimizing our prescription to minimize the observed RV dispersion (23 m s^{-1}) of our RV standard HIP 48331, a well-studied K5V star ($V = 7.7$) from the *Gaia*-RVs catalogue (Soubiran et al. 2013).

We also used the HIP 48331 data to predict the RV precision as a function of S/N. This was done by artificially degrading the 35 spectra of HIP 48331 to several specific lower S/N values and repeating the spectroscopic fitting analysis on each set. We then fitted a line to the ratio of the standard deviation of RVs (σ_{obs}) over the range of S/N values to the photometric uncertainty estimate as derived in Butler et al. (1996) to determine an empirically motivated correction to that relation, which we then use to determine the RV precision for each individual spectrum. The determined precisions range from $\sim 25 \text{ m s}^{-1}$ at very high S/N values, consistent with the above, to $\sim 100 \text{ m s}^{-1}$ at S/N of about 15.

We further verified the predicted precision using 60 unstacked spectra of bright science targets from individual nights. As described in section 5.2.1 ‘Sky Emission’ of B16, each epoch typically consists of three to five subsequently obtained spectra with S/N of 15–45 for targets with spectral type $\sim \text{K3–F5}$. Though these science targets may be affected by stellar jitter that biases the RV measurements, we expected this to introduce a constant systematic offset over the duration of these spectra and not increase the RV dispersion. We found good agreement with the relation determined using HIP 48331, though we saw some evidence that our preferred fitting approach is biased to the initial RV for stars with $v_r \sin(i) \gtrsim 30 \text{ km s}^{-1}$. We caution that our individual RV measurement errors may be underestimated by a factor of 2–4 in these cases, increasing with $v_r \sin(i)$, though note that this is a conservative bias (e.g. decreasing the likelihood of a false positive). While cross-correlating to obtain an initial RV estimate often alleviates the false minimum found by the optimizer, we suspect that a Bayesian analysis of our model would show the non-linear least-squares optimizer under-reports the errors in these cases. Due to the long Markov chain Monte Carlo (MCMC) run times, we have not yet performed this analysis.

Individual RV measurements (e.g. from each epoch) have a measurement error (σ_{meas}) that results from each fit and is computed using the empirically derived correction to the photometric uncertainty derived in Butler et al. (1996), which we determined using our observations of the RV standard HIP 48331 (see above). The uncertainty is, principally, a function of the S/N at each pixel and the slope of the line profiles in each fitted model. Further details and verification of our measurement errors can be found in section 5.2.1 of B16. This approach yields errors of more than 100 m s^{-1} at our pipeline S/N limit of 12 to a systematic limit of $\sim 25 \text{ m s}^{-1}$ at S/N levels above 200 for slowly rotating stars (see fig. 14 in B16).

3.2 Spectroscopic results

We report T_{eff} , $[\text{Fe}/\text{H}]$, $[\alpha/\text{Fe}]$, $v_r \sin(i)$, RV, σ_{obs} , σ_{meas} and the associated errors for our targets in Tables A1 and A2. The statistical uncertainties of the four stellar parameters were determined in B16 by looking at the distribution of best-fitting values relative to their multi-epoch means grouped into F, G and K bins. We found T_{eff} , $[\text{Fe}/\text{H}]$ and $[\alpha/\text{Fe}]$, and $v_r \sin(i)$ to have typical single-epoch

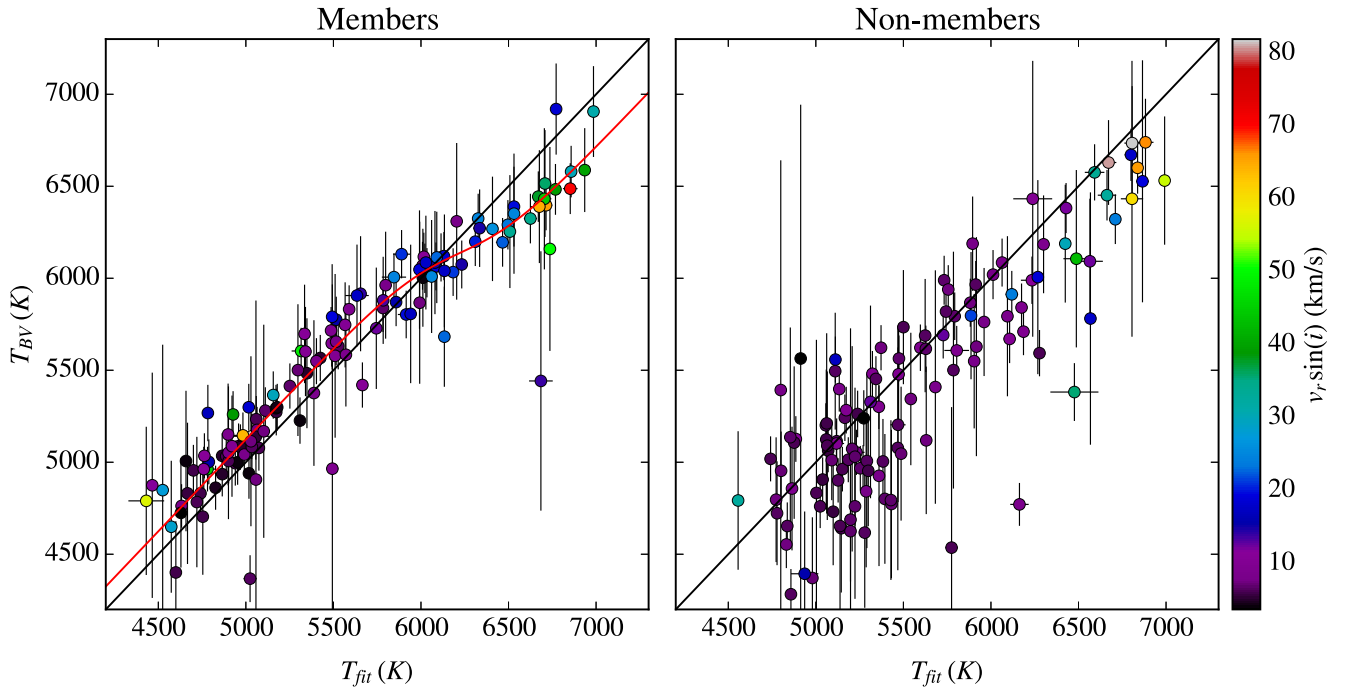


Figure 3. T_{eff} versus T_{B-V} for the combined cluster sample. Left: Values for stars with $P_{\text{RV}} \geq 50$ per cent (Section 5) plotted with coloured points indicating $v_r \sin(i)$. The red line represents our correction to Casagrande’s scale given in equation (2). Note that $\Delta(B - V)$ of 0.05 corresponds to $\Delta T \sim 100$ K here, about the level at which many members are offset below 6200 K, and perhaps suggesting a correction to $E(B - V)$. Right: Targets with $P_{\text{RV}} < 50$ per cent. Here, it seems the inapplicable reddening values for non-members enters into play. In both panels, the diagonal black line shows equivalence as a guide to the eye. Errors on T_{B-V} are dominated by photometric errors while errors on T_{eff} are as reported in this text.

precisions of 75 K, 0.05 dex and 0.75 km s^{-1} with a slight dependence on spectral type. The errors reported for T_{eff} , $[\text{Fe}/\text{H}]$, $[\alpha/\text{Fe}]$ and $v_r \sin(i)$ in Tables A1 and A2 are from table 7 of B16 corrected for the total number of epochs of each target (i.e. divided by \sqrt{N}) or the target’s standard error, whichever is greater. Typical precisions are ± 30 K, ± 0.02 dex and $\pm 0.3 \text{ km s}^{-1}$, exclusive of systematic effects, which are considered later in this section.

The systemic RVs are the inverse variance weighted ($\sigma_{\text{meas}}^{-2}$) means of our individual barycentre-corrected values. The errors on the means were determined by a Gaussian process resampling bootstrap and are typically around 40 m s^{-1} . In section 5.2 of B16, we found our measurements had an offset of $74 \pm 72 \text{ m s}^{-1}$ relative to the RV scale of Soubiran et al. (2013) when using five RV standards spanning the F5–K5 range. Given the compatibility of our reported errors, we do not expect there to be a significant unreported error component in our systemic RV values. We also report the mean of each target’s σ_{meas} values and the measurement variance ($\sigma_{\text{meas}}^{-2}$) weighted standard deviation of RV measurements for each target as σ_{obs} .

To measure the accuracy of T_{eff} , $[\text{Fe}/\text{H}]$ and $[\alpha/\text{Fe}]$, we compared our measurements for five slowly rotating standard stars spread across our effective temperature range with those in the literature (see table 3 in B16). We saw evidence that our T_{eff} values are cooler than literature values for both twilight solar and standard star spectra by 25–50 K, $[\text{Fe}/\text{H}]$ is low by -0.03 dex and $[\alpha/\text{Fe}]$ showed evidence of elevation at the 0.01 dex level. Note that these systematics are all within 2σ . We investigated the accuracy of our $v_r \sin(i)$ values by comparing them with those from Terndrup et al. (2002), with which we share 37 of our targets in NGC 2516. Our $v_r \sin(i)$ values agreed with a standard deviation of 2.2 km s^{-1} . We are unable to resolve values below $\sim 2 \text{ km s}^{-1}$, roughly 1/3 of our typical resolution element.

As an additional test of T_{eff} , we compared our values with $T_{\text{eff}}(B - V)$ values computed using the relation of Casagrande et al. (2010) and reddening-corrected colours (Table 1). For cluster members (see Section 5) with $T_{\text{eff}} < 6200$ K, we measured values about 100 K cooler than the reddening-corrected colour temperature. Above 6200 K, our values are about 250 K hotter (Fig. 3). To investigate if this shift in T_{eff} with T_{B-V} is correlated with the projected rotation, we artificially broadened the stellar lines of the F5V RV standard HIP 31415 [$v_r \sin(i) \sim 4.5 \text{ km s}^{-1}$] to simulate rotation values between 10 and 50 km s^{-1} and refitted the spectrum. At higher rotation rates, we see an elevation in T_{eff} and $[\text{Fe}/\text{H}]$ and a decrease in $[\alpha/\text{Fe}]$. For instance, at 40 km s^{-1} , we measure an increase in T_{eff} of 648 ± 163 K and $[\text{Fe}/\text{H}]$ of 0.2 ± 0.08 dex and a decrease of $[\alpha/\text{Fe}]$ by 0.11 ± 0.08 dex. We may see a slight elevation in T_{eff} at $\sim 10 \text{ km s}^{-1}$, though the uncertainty is quite large (Fig. 4). In general, for $v_r \sin(i) \lesssim 20 \text{ km s}^{-1}$, our stellar properties are largely unaffected.

Since the discrepancy in T_{eff} is plausibly a side effect of our analysis approach, we computed a model to shift our results on to the widely used scale of Casagrande et al. (2010). We quantified this effect for the combined set of cluster members in NGC 2516 and NGC 2422 by fitting a sigmoid to the difference in T_{eff} and T_{B-V} (Fig. 3):

$$T_{B-V} = T_{\text{eff}} + 124 \text{ K} - \frac{415 \text{ K}}{1 + e^{-0.0054 \text{ K}^{-1}(T_{\text{eff}} - 6220 \text{ K})}}. \quad (2)$$

One plausible explanation for equation (2) is a combination of an $E(B - V)$ overestimate of ~ 0.05 in both clusters and a tendency of our pipeline to overestimate T_{eff} for more rapidly rotating stars; 66 per cent of stars with a corrected $T_{\text{eff}} > 6200$ K have $v_r \sin(i) > 25 \text{ km s}^{-1}$. Non-member stars show a generally linear, albeit offset, agreement with T_{B-V} and are typically 195 ± 54 K

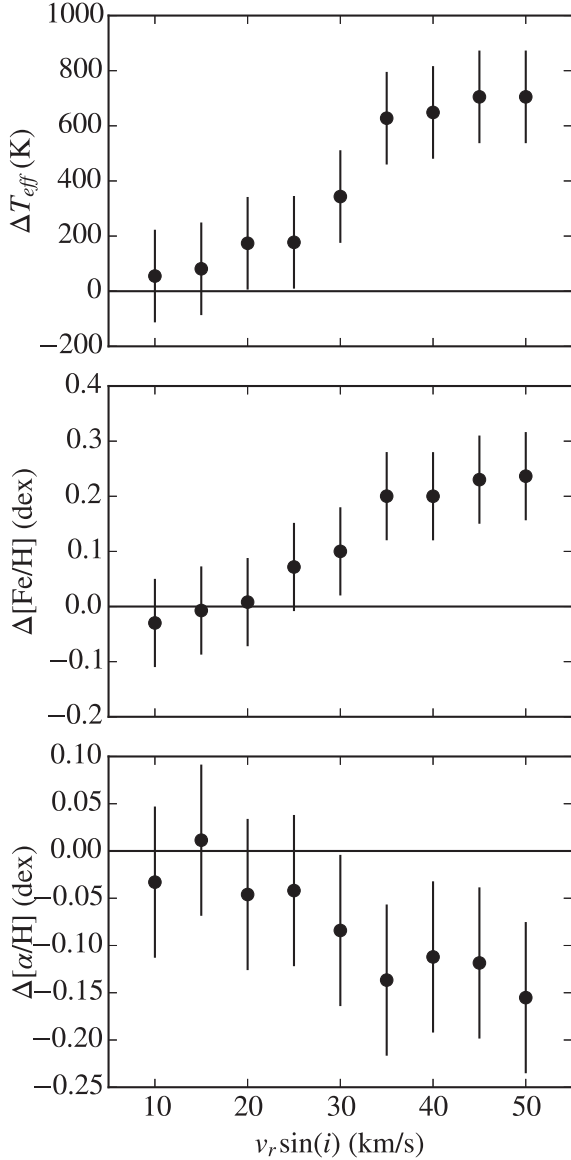


Figure 4. T_{eff} , [Fe/H] and $[\alpha/\text{Fe}]$ measurements are affected by artificially broadening the stellar lines in the spectrum of our F5V standard HIP 31415. Error bars show 1σ confidence intervals. We stress that we do not see this behaviour in cooler stars.

hotter than their T_{B-v} values despite their on average lower $v_r \sin(i)$. We have applied the sigmoid correction to the values we report for members and probable members.

4 SPECTROSCOPIC BINARIES

The 9–12 epochs of precise RVs obtained with spacings from ~ 1 d to ~ 1 yr allow us to identify stars orbited by stellar and near-stellar companions. Because of stellar-activity-induced RV variability (see Section 7), some stars with RV variations above our measurement uncertainty, σ_{meas} , may not have an orbiting companion. We, thus, select a variability threshold to help delineate between clear binaries and less obvious cases.

Fig. 5 shows the distribution of σ_{meas} and σ_{obs} for all stars targeted in NGC 2516 and NGC 2422 barring stars mentioned in Section 5.1. The distribution of σ_{meas} shows a Poisson-like peak at $\sim 60 \text{ m s}^{-1}$, a tail that extends to $\sim 250 \text{ m s}^{-1}$, and then a scattering of stars with

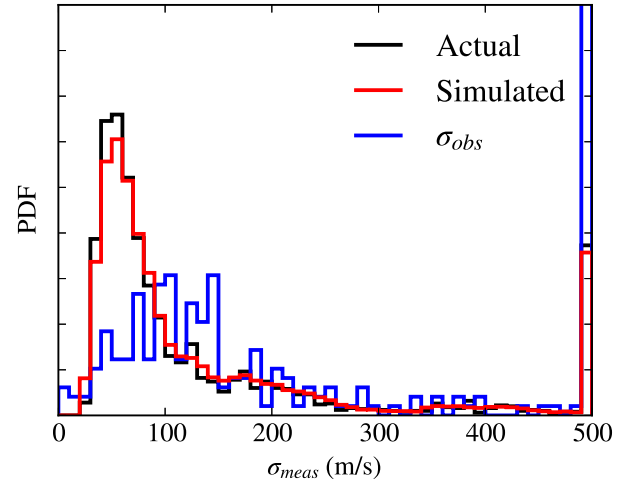


Figure 5. The black line shows the distribution of measurement errors, σ_{meas} , for spectra of photometric and candidate members in our sample, exclusive of the seven continuum stars listed in Section 5.1. The red line is the distribution of simulated σ_{meas} values we generate for our companion simulations. The discrepancy to the left of the peak is caused by a higher variance in individual σ_{meas} values for stars with the smallest mean σ_{meas} than our error simulation code captures. The distribution of σ_{obs} is shown for comparison in blue. Its peak in the 500 m s^{-1} bin is ~ 3.4 times those of the other two. Values above 500 m s^{-1} have been clipped to that value for this plot. Note that all three histograms have very different normalizations.

larger σ_{meas} . The distribution of σ_{obs} shows a broad distribution from 50 to 150 m s^{-1} , a tail that roughly matches σ_{meas} , and an excess of stars above 500 m s^{-1} , which is ~ 3.4 times that expected from measurement errors alone.

Under the assumption that most stars have constant RVs, the difference between the peaks of the σ_{meas} and σ_{obs} distributions can serve as a proxy for the characteristic amplitudes of any stellar-activity-induced RV variability. Based on this comparison, we adopt a stellar variability

$$\sigma_{\text{stel}} \equiv \sqrt{\sigma_{\text{obs}}^2 - \sigma_{\text{meas}}^2}$$

where $\sigma_{\text{stel}} = 300 \text{ m s}^{-1}$ is the dividing line between what we will refer to as spectroscopic single and spectroscopic binary stars in our sample. We emphasize that, as defined, these spectroscopic binary stars could have brown dwarf ($M \leq 0.07 M_{\odot}$) or planetary ($M \leq 13 M_{\text{Jup}}$) companions. We also require that the RV variability is statistically significant (Section 8) to account for the small number of stars with large measurement errors.

We identified 40 spectroscopic binaries in our sample of 126 stars in the field of NGC 2516 and 22 in our sample of 125 stars in the field of NGC 2422. We find a median σ_{obs} of 3200 m s^{-1} , with values ranging from 310 to 38000 m s^{-1} . Eight each have $\sigma_{\text{obs}} = 300\text{--}500 \text{ m s}^{-1}$ and $\sigma_{\text{obs}} = 500\text{--}1000 \text{ m s}^{-1}$ with the remainder being above 1000 m s^{-1} . Eight of our spectroscopic binaries (four in each cluster field) are clear double-lined binaries. The parameters we report are for the stronger of the pair, but errors for these stars should be treated with a degree of caution. We exclude five stars with $\sigma_{\text{stel}} > 300 \text{ m s}^{-1}$ that have $\sigma_{\text{meas}} > 600 \text{ m s}^{-1}$ and $v_r \sin(i) > 35 \text{ km s}^{-1}$ as their RV variations were not statistically significant ($P_v \leq 0.96$; Section 8). We use the codes B or SB2 to denote spectroscopic or double-lined spectroscopic binaries, respectively, in Tables A1 and A2. We are able to recover candidate periods for a number of these binaries in Section 8.1. RV curves for these stars are provided in Appendix B (online only).

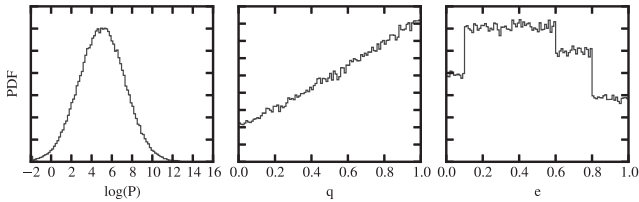


Figure 6. The period, mass ratio and eccentricity distributions of stellar binaries in our companion simulations. Though not evident in the plot, the mass ratio and eccentricity distributions are a function of the period. Distributions are based on those given in [DK13](#).

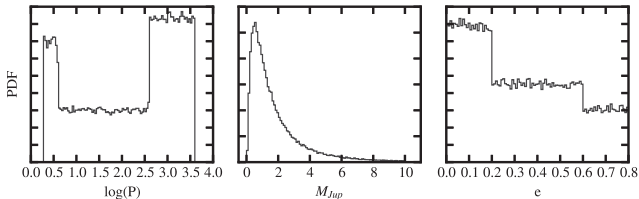


Figure 7. The period, mass ratio and eccentricity distributions of exoplanetary companions in our companion simulations. Distributions are based on those given in [Udry & Santos \(2007\)](#).

4.1 Companion simulations

The temporal sampling and precision of our survey prevented us from detecting long-period variables and the lowest mass companions. To investigate these factors and their effects upon both the binary criterion described above and the results presented in later sections, we performed Monte Carlo simulations of binary stellar and exoplanetary systems. Here, we describe the technical aspects of our simulations; later sections use these simulations to consider the RV variability we would expect, to quantify companion detectability and to investigate how likely binaries are to pass our membership tests. [Figs 6 and 7](#) show the input distributions for period, eccentricity and companion mass for the binary and exoplanet populations. These are according to [Duchêne & Kraus \(2013, hereafter DK13; for binaries\)](#) and [Udry & Santos \(2007, for exoplanets\)](#). We chose a total exoplanet fraction such that we would expect 1.2 per cent of stars to have hot Jupiter companions consistent with [Wright et al. \(2012\)](#), and we start with a binary fraction of 45 per cent consistent with [DK13](#). We adjust this value when investigating the binary fraction.

We simulated a sample of 150 000 systems around a $1 M_{\odot}$ star with carefully generated measurement errors for each simulated RV to match the properties of our data set. These errors were generated by creating a sample of fake mean σ_{meas} values from the distribution of σ_{meas} values in our data. We then sampled a Gaussian distribution with width corresponding to the mean spread in σ_{meas} for each target ($\sim 10 \text{ m s}^{-1}$) to perturb the fake errors chosen for each star. In this way, we generated unique errors on each simulated RV measurement that mirror our sample (see the red line in [Fig. 5](#)). We observe each simulated star at the sample cadence of each cluster by sampling Gaussians located at each RV where each Gaussian is given the width of the corresponding simulated error and computed σ_{obs} (Section 3.2) and P_v (Section 8) for each simulated target. When investigating how binaries fare in our membership test, we included random systemic velocities for each star using our observed cluster velocity dispersions of 734 m s^{-1} in NGC 2516 and 750 m s^{-1} in NGC 2422 (Section 6).

We find our 300 m s^{-1} binarity threshold will identify 69 per cent of the stellar binaries in our sample as single members, though

95 per cent these have periods longer than 25 yr. Similarly, we find the threshold imposes a 9 per cent false-positive rate (with stated binary and exoplanet fractions, which are lower with increasing binary fraction), 1/5 of which (1.8 per cent of the total) would be (very massive) planetary or brown dwarf companions flagged as binaries.

5 MEMBERSHIP

Because stars in an open cluster are expected to have formed at the same time and from the same parent cloud, and to still be moving through space together, numerous age, compositional and kinematic diagnostics can be used to identify cluster members. While multiple diagnostics will, in general, improve the overall accuracy of membership lists, their use can also lead to the exclusion of stars in peculiar evolutionary or dynamical stages (e.g. interacting star–star or star–planet systems). Since RVs were not used in identifying cluster members from [J01](#) or [P03](#), the precise RVs achieved in this study provide a very valuable check on membership.

We determine membership probabilities by assuming that the RVs of the stars in our sample are drawn either from a Gaussian RV distribution centred on the cluster (for members) or from a Besançon distribution ([Robin et al. 2003](#)) of Galactic stars along the cluster line of sight (for non-members). The Besançon distribution is a Galactic stellar-population synthesis model that provides broad agreement with surveys and includes kinematics. To compute the RV membership probability, $P_{\text{RV}}(v)$, we first computed an observed probability density function (PDF) from the normalized sum of Gaussian PDFs for each of our target stars. That is, we locate a Gaussian at each measured RV with σ corresponding to the bootstrapped errors on the weighted mean ([B16](#)). We then fitted the PDF with a weighted sum of a Gaussian and the Besançon PDF and computed a membership probability for each star using

$$P_{\text{RV}}(v) = \frac{f_{\text{cluster}}(v)}{f_{\text{cluster}}(v) + f_{\text{MW}}(v + c)}, \quad (3)$$

where $f_{\text{cluster}}(v)$ is the fitted Gaussian PDF component and $f_{\text{MW}}(v + c)$ is the Milky Way component with a constant to allow for small shifts in the centre of the distribution. We adopt targets with $P_{\text{RV}} > 50$ per cent as RV members such that the balance of probability is for membership. This threshold corresponds to $\sim 2.5\sigma_{\text{RV}}$ in both clusters. [Figs 8 and 9](#) show histograms of our target RVs and the Besançon RVs, our PDF and the best-fitting model, and a comparison of the resulting cumulative distribution functions. Considering the overlap of the best-fitting Besançon and Gaussian RV distributions for each cluster, we expect this to yield a false-positive rate of 12 per cent in NGC 2516 and 13 per cent in NGC 2422. This fitting process also yields values for each cluster’s observed velocity dispersion (Gaussian sigma), which we discuss in Section 6.

Our Monte Carlo simulations show this membership test is strongly biased against large-amplitude RV variables. At our observing cadence – for either cluster – 30 per cent of the time we would observe a simulated binary system to have $P_{\text{RV}} < 50$ per cent. Large-amplitude binaries, e.g. those we identify as spectroscopic binaries, fare much worse: ~ 67 per cent of simulated systems we flag as an RV binary will fail a $P_{\text{RV}} = 50$ per cent cut. To adopt a more forgiving approach, we consider stars with $\sigma_{\text{stel}} > 300 \text{ m s}^{-1}$ that have RV within $2\sigma_{\text{RV}}$ of the $P_{\text{RV}} = 50$ per cent threshold to be probable members. This relaxed criterion reduces the exclusion of large-amplitude binaries from 67 per cent to 31 per cent in our simulation.

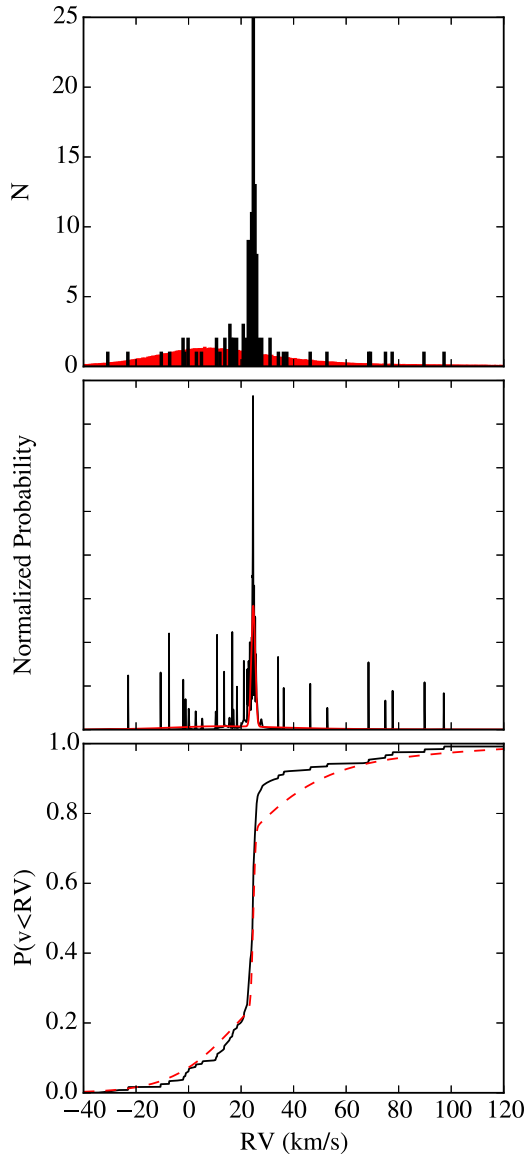


Figure 8. Top: Histogram of the measured RVs of our targets in NGC 2516 superimposed over a scaled histogram of stars in a Besançon model along the line of sight to NGC 2516 with matching cuts on V and $B - V$. Middle: PDF constructed from our RVs and their measurement errors. Our best-fitting model is drawn as a solid red line. Bottom: The continuous distribution functions for our PDF (solid) and the best-fitting model (dashed). The discrepancy to the right of the cluster is a result of fewer contaminants than predicted by the Besançon model.

The results of the membership analysis are summarized in the following sections. A small number of stars could not be tested for membership using the procedure outlined or are otherwise notable despite their RV non-member status and are described in Section 5.1. Membership and the short-period multiplicity of stars in NGC 2516 and NGC 2422 are discussed in Sections 5.2 and 5.3, and a candidate association, perhaps related to the Monoceros ring, in Section 5.4. The membership probabilities, P_{RV} , are listed in Tables A1 and A2. We use the codes N (non-member), P (probable member) and M (member) to denote the levels of RV membership certainty. Two stars described in the following section are given the code X, as no determination was possible.

5.1 Continuum stars and probable contaminants

Twenty-seven stars exhibit a diffuse interstellar band (DIB) at 7224.2 \AA (Fig. 10 and Herbig & Soderblom 1982). None of the 22 for which we are able to obtain RVs pass our RV membership test, suggesting that there is insufficient column depth within a few hundred parsecs to produce a notable feature. This suggests that the presence of the DIB indicates a non-member target. The diffuse band does not pose any difficulty to our fits, nor does it perturb our results, as verified by masking out the region. We do find that stars with the feature generally yield lower $\log(g)$ values relative to cluster members if we allow $\log(g)$ to vary, further suggesting they are distant giants.

Five stars exhibiting the DIB and with colours corresponding to mid-F and late-G/early-K spectral types have either few, exceptionally broad or no discernible lines (Fig. 10) and caused our fitting pipeline to fail. A visual comparison with the most rapid rotators that we are able to fit ($\sim 90 \text{ km s}^{-1}$) suggests two of these (147-012316 and 147-012471) would require $v_r \sin(i) \sim 120 \text{ km s}^{-1}$ for an approximate match with the template spectrum. The remaining three show no evidence of any photospheric absorption features, even when compared to templates with $v_r \sin(i) \sim 200 \text{ km s}^{-1}$. Tables A1 and A2 give the parameters for these stars as missing data with type C for continuum, as we are not able to fit their spectra and we flag them as non-members due to the DIB. Note that these could be heavily extinguished, background early-type stars that would not have appreciable lines in this region independent of rotation, which would also be expected. One star was observed using a fibre with very poor throughput and never attained sufficient S/N for analysis. It is noted with an X for both type and membership. We now describe some specific properties of the targets that have exceptionally weak or scarcely discernible lines.

146-012353 is listed by J01 as photometric single member 6337 in NGC 2516. It has $T_{B-V} = 6900 \text{ K}$. It is 0.08 arcsec from a source given in Damiani et al. (2003, hereafter D03) as having $\log(L_X) < 29.75 \text{ erg s}^{-1}$ based on *Chandra* observations. Visual inspection suggests $v_r \sin(i)$ in excess of 200 km s^{-1} .

147-012316 is listed by J01 as photometric single member 8920 in NGC 2516. It has $T_{B-V} = 6840 \text{ K}$. D03 reports it as having a flux of $1.36 \pm 0.48 \times 10^{-6} \text{ counts s}^{-1} \text{ cm}^{-2}$ and $\log(L_X)$ of 28.85 erg s^{-1} . Visual inspection suggests $v_r \sin(i)$ is between 120 and 150 km s^{-1} .

147-012471 is listed by J01 as photometric single member 12302 in NGC 2516. It has $T_{B-V} = 6625 \text{ K}$. It is 0.134 arcsec from a source in D03 with $\log(L_X) < 29.96 \text{ erg s}^{-1}$ and 0.282 arcsec from source 272 of Pillitteri et al. (2006), which is reported to have a MOS1 equivalent count rate of $2.18 \pm 0.23 \text{ counts s}^{-1}$ with the *XMM-Newton* EPIC camera. Visual inspection suggests $v_r \sin(i)$ of $\sim 120 \text{ km s}^{-1}$.

378-036424 is listed as member 956 in NGC 2422 by P03 and has $T_{B-V} = 5650 \text{ K}$. Visual inspection suggests $v_r \sin(i)$ in excess of 200 km s^{-1} .

379-036213 is one of our 25 UCAC4 targets and has $T_{B-V} = 5330 \text{ K}$. Visual inspection suggests $v_r \sin(i)$ in excess of 200 km s^{-1} .

We also note one metal-poor high-velocity star in the NGC 2516 sample. **146-012596** has an RV of $335.901 \pm 0.048 \text{ km s}^{-1}$ and does not show any sign of RV variability. We find a rotation rate of 3.1 km s^{-1} and note that its iron abundance runs into the lower edge of our grid, suggesting the true value may be less than -1 dex . It exhibits the DIB at 7224 \AA .

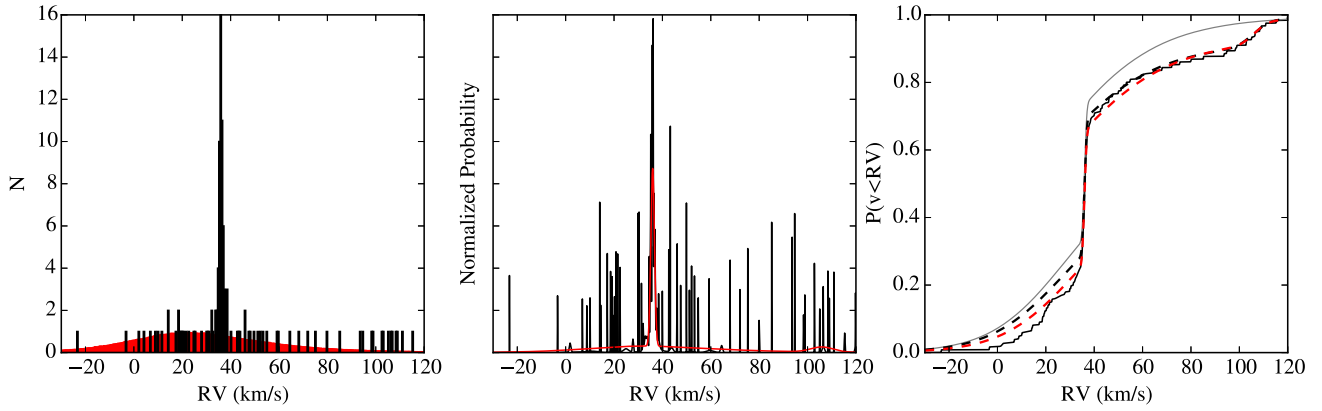


Figure 9. Left: Histogram of the measured RVs of our targets in NGC 2422 superimposed over a scaled histogram of stars in a Besançon model along our pointing’s line of sight with matching cuts on V and $B - V$. Middle: PDF constructed from our RVs and their measurement errors. Our adopted model is plotted as a red line. Right: The continuous distribution functions for our data (solid) and the best-fitting models. The thin grey line is for a simple Besançon + Gaussian model. The dashed black line includes a second Gaussian for the overdensity of stars at $\sim 106 \text{ km s}^{-1}$ and the dashed red line includes both the second Gaussian and an allowance for a mean shift (measured to be -4.9 km s^{-1}) in the Besançon RVs. The modifications alter P_{RV} by no more than 1.2 per cent with a mean of 0.2 per cent and do not affect the classifications of any of our stars.

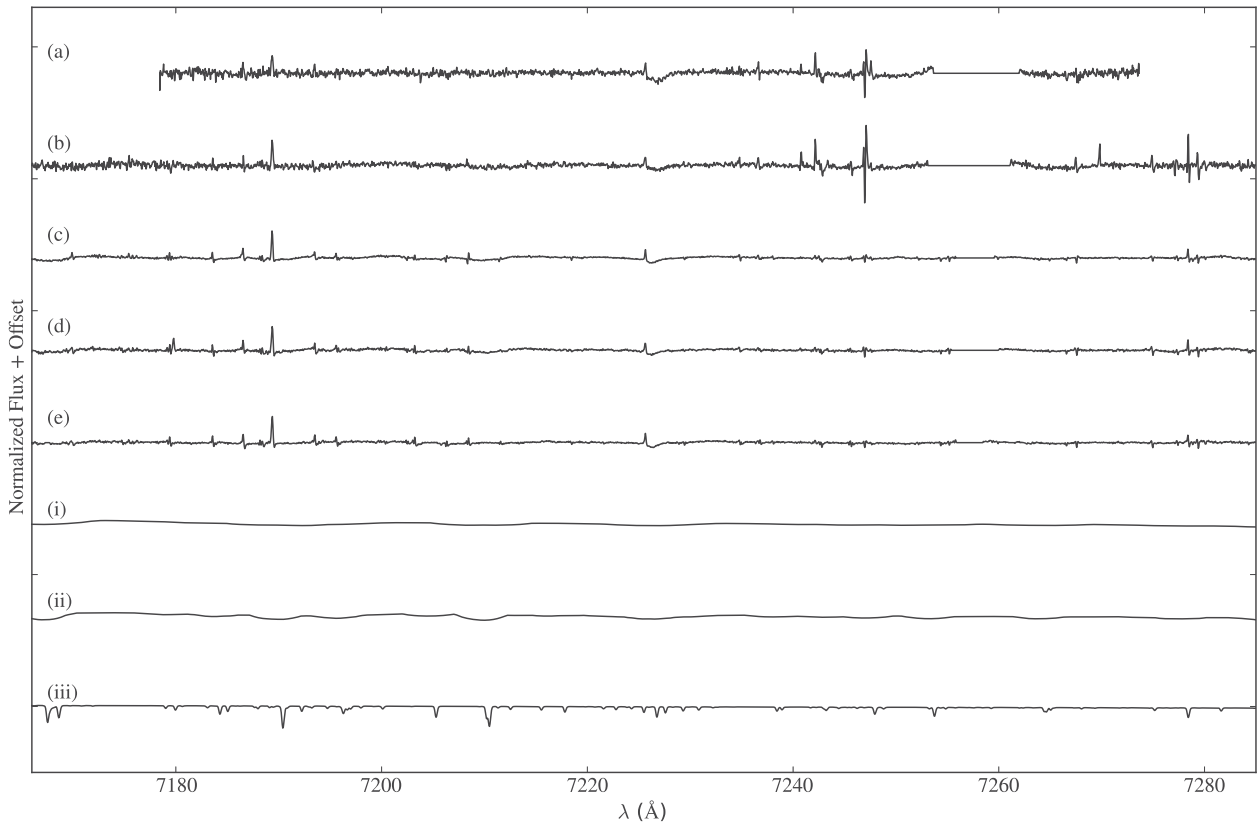


Figure 10. Spectra (a–e) of the five near featureless objects in our sample. The individual epochs have been (mostly) cleaned of telluric absorption and emission lines and summed to yield these high S/N spectra. The spectrum of 379-036213 (a) is clipped at either end as the data in some of the component epochs fall below our minimum S/N limit for fitting. A DIB is visible in the spectra at 7224 \AA . The spectra are as follows: (a) 379-036213: $V = 14.2$, $B - V = 0.87$, $S/N = 150$. (b) 378-036424: $V = 15.0$, $B - V = 0.75$, $S/N = 79$. (c) 147-012471: $V = 12.0$, $B - V = 0.53$, $S/N = 364$. (d) 147-012316: $V = 11.7$, $B - V = 0.47$, $S/N = 336$. (e) 146-012353: $V = 11.7$, $B - V = 0.46$, $S/N = 343$. Visually, 147-012471 and 147-012316 (c and d) have faint features, suggesting they are rotating rapidly. The bottom three spectra (i–iii) are all $T_{\text{eff}} = 6800 \text{ K}$ solar abundance PHOENIX templates and have been broadened to $v_r \sin(i)$ of (i) 200 km s^{-1} , (ii) 100 km s^{-1} and (iii) 20 km s^{-1} for comparison.

Finally, **378-036788** is identified by **P03** as an early-type member in NGC 2422. This star entered our sample via a cross-matching error and has no discernible features. We list it as type C in Table A2 with a membership flag of X for no data.

5.2 Membership and short-period multiplicity in NGC 2516

Of the 126 photometric members targeted in NGC 2516, we identified 81 stars as RV members. Of these 81, we classify 54 as RV

single and 27 as RV binary. Two RV members are labelled photometric non-members by J01 (146-012470 and 147-012335, each failing one of J01's three tests). 12 of the RV members are classified by J01 as photometric binaries. Ten of the 51 J01 single members fail our RV membership cut. J01 estimated contamination fractions of 15 ± 8 per cent for single and 30 ± 11 per cent for binary members in their membership list over the relevant colour range and thus, we could reasonably expect to find RV non-members at this level. Our simulation predicts 11 per cent of true cluster members will be excluded by our membership test assuming cluster members have (systemic) Gaussian RVs distributed according to the measured cluster velocity dispersion (734 m s^{-1} ; Section 6). 37 per cent of the excluded members are predicted to be binaries with 99 per cent (95 per cent) having $P > 8.6$ (25) yr.

Eight of the RV binary members were included by our relaxed membership criterion and 18 were identified as single members in J01. We find 29 of the photometric binaries in J01 fail our RV binarity test and 17 fail our RV membership cut. After correcting for our sensitivity, our findings agree with their contamination estimates for single members but find they underestimate the photometric binary contamination by ~ 22 per cent, assuming our RV membership is correct.

Using the RV binary criteria described in Section 4, we find an observed RV binary fraction of 33 ± 5 per cent. Our sample is subject to a false-positive rate of 9 per cent on RV binarity and false positive and false-negative rates of 12 per cent and 31 per cent, respectively, on RV membership. This suggests that four of the non-member RV binaries are RV members, two of the 27 RV binary members are single members, and three of the 27 are binary but not members. With these corrections, we would predict $25 [\approx 0.91 \times (27 + 0.31 \times 13 - 0.12 \times 27)]$ RV binaries with $\sigma_{\text{stel}} > 300 \text{ m s}^{-1}$ in a sample of 78 $[\approx 81 - 0.12 \times 81 + 0.31 \times 13 + 0.05 \times 28]$ RV members for an observed RV binary fraction of 32 ± 6 per cent.

Our companion simulation, presented in Section 4.1, predicts only 15 per cent of stars should be flagged as RV binary ($\sigma_{\text{stel}} > 300 \text{ m s}^{-1}$) under the assumption that the overall binary fraction is 45 per cent, matching the field population. We would expect 27 per cent flagged at an overall binary fraction of 85 per cent as reported in J01. A 100 per cent binary fraction would result in 31 per cent of stars being flagged as RV binary, consistent with what is measured here. We caution that this assumes the same period distribution as that in the field. For comparison, in J01, 47 of our 126 targets (37 per cent) were flagged as photometric binaries, though recall we do not flag 12 of their photometric binaries as RV binaries. We investigate the potential composition of these binaries in Section 8.

Extensive work in the field shows typical multiplicity fractions of 62 ± 3 per cent for solar-mass stars ($0.7\text{--}1.3 M_{\odot}$; see the review in DK13) and work on open clusters has shown a similar picture with a value of about 65 per cent (DK13). Our result is consistent with J01's finding of 85 ± 15 per cent, especially considering that mass segregation may be influencing our finding, as all of our targets are near the cluster centre. Indeed, a perusal of cluster colour-magnitude diagrams in, for example, the WEBDA data base will quickly reveal how striking the binary sequence is in NGC 2516.

Of the 41 RV non-members, 13 are identified as spectroscopic binaries, one of which is a double-lined binary. Six of our RV spectroscopic binary non-members were listed by J01 as photometric single members and eight as photometric binary members. We are unable to assess fully the membership status of the three featureless stars in NGC 2516 (Section 5.1). Although J01 classified them as

single members, we classify them as RV non-members due to the DIB.

5.3 Membership and short-period multiplicity in NGC 2422

Of the 100 photometric members and 25 candidate members targeted in NGC 2422, we identified 57 stars as RV members, 11 of which are RV binary. Of the 25 candidate members, we find seven to be RV single members and five to be RV binary members. P03 does not attempt to identify binaries using their photometry, so we are unable to compare our results, as in NGC 2516. Five RV binaries were included by our relaxed RV binary membership criterion. Our simulation predicts 14 per cent of true cluster members will be excluded by our membership test, assuming cluster members have (systemic) Gaussian RVs distributed according to the measured cluster velocity dispersion (Section 6). 37 per cent of the excluded members are predicted to be binaries with 99 per cent (95 per cent) having $P > 8$ (23) yr.

Note seven stars – 378-036692, 378-036906, 379-035967, 379-035982, 377-035049, 378-036136 and 378-036960 – pass our membership test but are somewhat removed from the rest of the main sequence (MS) in the temperature–magnitude space (Fig. 11): three are below and four above. The relative areas of the Besançon and cluster Gaussian PDFs suggest that we could expect seven field stars to pass as RV members. All but 378-036960 yield $\log(g)$ values broadly consistent with MS stars if we allow $\log(g)$ to vary and we also note 378-036960 is one of only two mid-F stars that pass our membership test and have $v_r \sin(i) \lesssim 25 \text{ km s}^{-1}$. Two of the seven, 378-036692 and 379-035967, were flagged as members by P03. The rest were targets selected from UCAC4. Three of them – 378-036906, 378-036136, 378-036960 – have errors of $B - V$ in excess of 0.13 mag. We flag these three stars as probable members instead of members.

Based on the RV binary criteria described in Section 4, we find an observed RV binary fraction of 19 ± 5 per cent. With a false-positive rate of 9 per cent on RV binarity and false-positive and false-negative rates of 13 per cent and 31 per cent, respectively, on RV membership, we expect that three of the 11 non-member RV binaries are, in fact, RV binary members, one of the 11 member RV binaries is not binary, and one of the 11 RV members is not a member. With these corrections, we would predict 12 RV binaries with $\sigma_{\text{stel}} > 300 \text{ m s}^{-1}$ in a sample of 59 RV members for an observed RV binary fraction of 20 ± 5 per cent. Our simulation predicts a cluster binary fraction of 62 ± 16 per cent would produce our observed RV binary fraction, perfectly consistent with DK13. We investigate the potential composition of these binaries in Section 8.

Of the 68 RV non-members, 11 are RV binaries, two of which are double-lined binaries. We are unable to assess fully the status of the two previously mentioned featureless stars (one from P03 and one from UCAC4) in NGC 2422. We classify them as RV non-members due to the DIB.

5.4 A distant association

In NGC 2422, we noted an overdensity of 11 stars with a mean RV of $\sim 107 \text{ km s}^{-1}$, well removed from the cluster and the Besançon model distribution. We introduced an additional Gaussian component to our membership model that accounted for this grouping and substantially improved our continuous distribution function (Fig. 9). Note that the second Gaussian does not appreciably affect our membership probabilities in NGC 2422. These stars cluster at $106.8 \pm 1.3 \text{ km s}^{-1}$ with σ_{RV} of 3.76 km s^{-1} . They have a mean

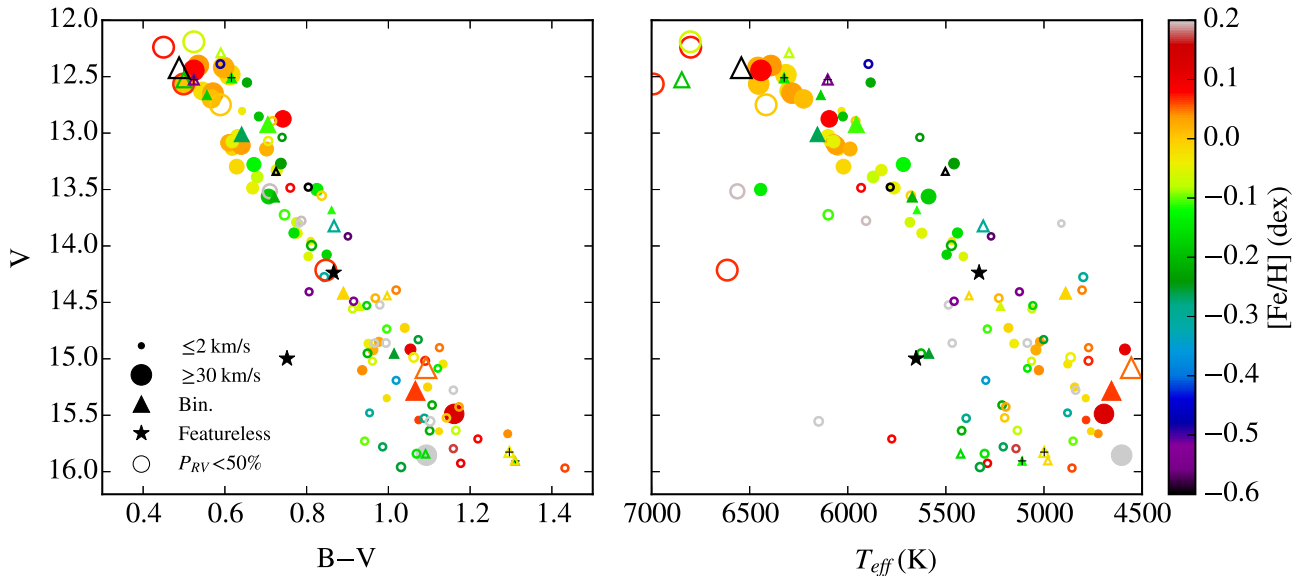


Figure 11. Colour–magnitude (left) and temperature–magnitude (right) diagrams for targets in NGC 2422. Stars we identified as RV members (Section 5) are shown as filled circles or, for RV binaries, triangles. Double-lined binaries have a tiny black plus sign on them. The colour indicates $[\text{Fe}/\text{H}]$ and the point size $v_r \sin(i)$. Unfilled points show the same for targets that do not pass our RV membership test. The filled black stars correspond to the featureless spectra discussed in Section 5.1 and are plotted using T_{B-V} . We have corrected the T_{eff} values of RV members using equation (2).

Table 5. Cluster properties.

Cluster	N	RV (km s^{-1})	σ_{RV} (m s^{-1})	$[\text{Fe}/\text{H}]$ (dex)	$[\alpha/\text{Fe}]$ (dex)	Binary fraction (percentage)
NGC 2516	81	24.50 ± 0.12	734 ± 104	-0.08 ± 0.01	0.03 ± 0.01	100^{+0}_{-15}
NGC 2422	57	35.97 ± 0.09	750 ± 65	-0.05 ± 0.02	0.02 ± 0.01	62 ± 16

$v_r \sin(i)$ of $3.9 \pm 0.7 \text{ km s}^{-1}$ and all exhibit a DIB at 7224.2 \AA . When fitting allowed $\log(g)$ to vary, we found values ~ 2.25 dex lower than cluster members in NGC 2422. As a second test, we fitted them using the pipeline of Walker, Olszewski & Mateo (2015), which indicated $\log(g)$ of 0.5–1.5. These tests strongly suggest the stars are giants or supergiants, though there is no star formation at the required distance for a supergiant. Assuming 1.22 mag of extinction and 0.39 mag of reddening as per Schlafly & Finkbeiner (2011), an average V magnitude of 15.5, and a dereddened colour temperature of $\sim 5500 \text{ K}$, we would suggest that these stars are either G2 supergiants at 150 kpc or G5 giants at $\sim 13 \text{ kpc}$. NGC 2422 is located at $l = 231$, $b = +3$ and it is possible that these stars may be part of some stream or ring along the line of sight. Note that the Monoceros ring is at higher Galactic latitudes (Slater et al. 2014) and it is, thus, possible that this represents a detection of that material at a lower latitude where detection with photometry is impractical due to confusion with the disc.

6 CLUSTER RVs, METALLICITY AND PROJECTED ROTATION

We now turn our attention to the aggregate properties of our targeted clusters: systemic RV, observed velocity dispersion, iron and α -element abundances, and binary fractions.

The systemic RV for each cluster was computed in the same manner as that for each target (Section 3.2), excluding both RV non-members and the small number of RV members included by our relaxed RV membership criterion. The cluster velocity dispersions are the Gaussian standard deviation taken from our fit of

equation (3) as described in Section 5. These values are reported in Table 5. Our RV for NGC 2516 agrees with the result of Terndrup et al. (2002) but the authors do not report a velocity dispersion for the cluster. We are the first authors to report detailed RV data for NGC 2422.

$[\text{Fe}/\text{H}]$ and $[\alpha/\text{Fe}]$ values were derived using a Gaussian kernel density estimation on the member stars (Figs 12 and 13). Values are reported in Table 5. In NGC 2516, our iron abundance of -0.08 ± 0.01 dex is only slightly inconsistent with the value of 0.01 ± 0.07 dex reported by Terndrup et al. (2002) using the spectroscopy of two stars, neither of which is in our sample. We measure an α -element enhancement of 0.03 ± 0.01 dex, though we acknowledge this value may be driven down by our optimizer’s interaction with the high rotation rates in hotter stars (Fig. 4). In NGC 2422, our iron abundance of -0.05 ± 0.02 dex is moderately inconsistent with the $+0.11 \pm 0.1$ dex value reported by Nissen (1988) using Strömgren photometry of 11 stars. We measure an α -element enhancement of 0.02 ± 0.01 dex.

We separated both $[\text{Fe}/\text{H}]$ and $[\alpha/\text{Fe}]$ into spectral-type groups to investigate any trends with temperature, as is illustrated in Figs 12 and 13. In both clusters, we measured lower iron abundances for G stars than the cluster as a whole (-0.04 ± 0.022 dex for NGC 2516 and -0.04 ± 0.028 dex for NGC 2422) and also note elevated abundances in F stars, especially in NGC 2516 ($+0.07 \pm 0.022$ dex). This latter point is expected given the higher stellar rotation and its effect on our $[\text{Fe}/\text{H}]$ values (Section 3.2 and Fig. 4). α -element abundances present a more complicated picture with some indication of bimodality in all spectral-type bins. We posit this indicates our data may benefit from a traditional abundance analysis to test

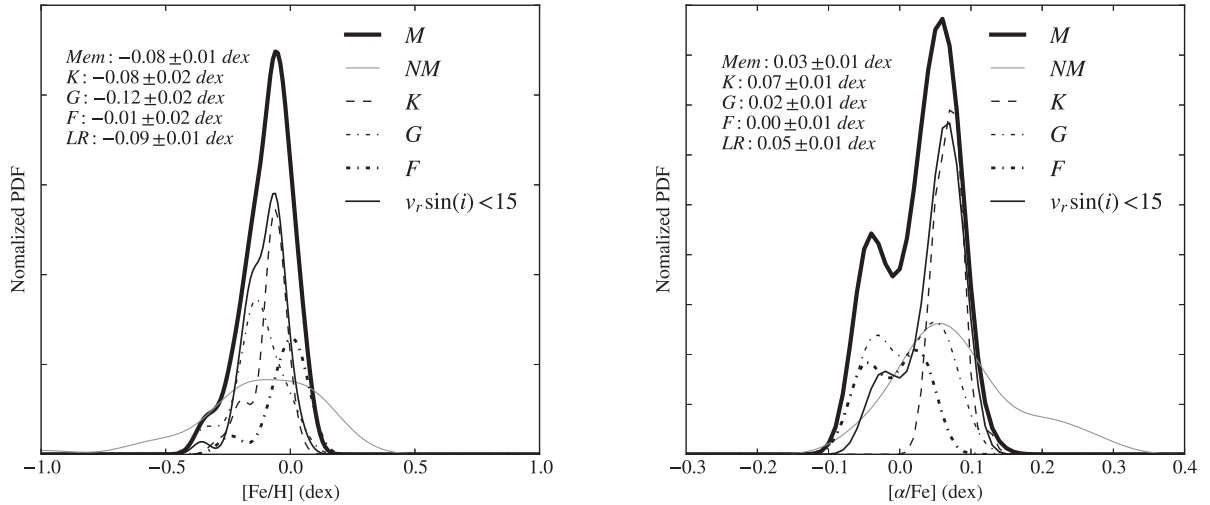


Figure 12. Gaussian kernel density estimates of $[\text{Fe}/\text{H}]$ (left) and $[\alpha/\text{Fe}]$ (right) in NGC 2516. The thick black line shows the full RV member population and the thin grey line the RV non-member sample. The other lines show the distributions for various subsets of our RV member sample. LR stands for low-rotation and gives the mean for the $v_r \sin(i) < 15 \text{ km s}^{-1}$ RV member sample.

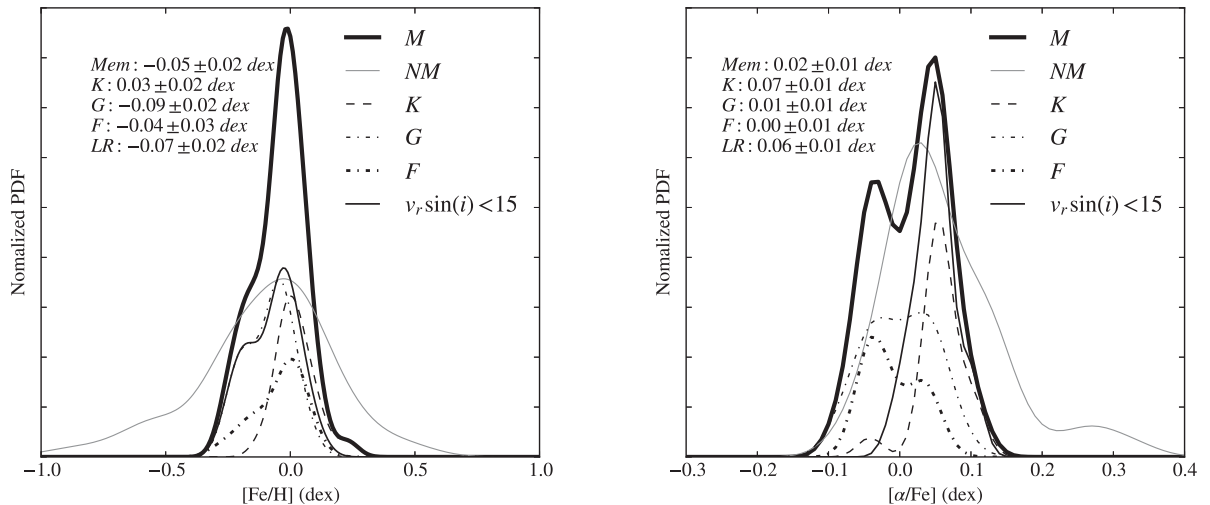


Figure 13. Gaussian kernel density estimates of $[\text{Fe}/\text{H}]$ (left) and $[\alpha/\text{Fe}]$ (right) in NGC 2422. The thick black line shows the full RV member population and the thin grey line the RV non-member sample. The other lines show the distributions for various subsets of our RV member sample. LR stands for low-rotation and gives the mean for the $v_r \sin(i) < 15 \text{ km s}^{-1}$ RV member sample.

for systematics in our science targets not present in our standard stars [e.g. due to their uniformly low $v_r \sin(i)$].

Figs 14 and 15 plot the distribution of stellar rotation with T_{eff} . These figures show uniformly elevated rotation rates in F stars and a general decline with spectral type, but also a spread among K stars. For comparison, we also show the distribution for the similarly aged Pleiades ($\sim 100 \text{ Myr}$, see e.g. Queloz et al. 1998). Our distributions for both clusters appear consistent with the overall trend with T_{eff} seen in the Pleiades data, though we do not see elevated rotation in G stars and see a greater spread among K stars.

A simplistic Monte Carlo resampling simulation where we draw with replacement from our sample until we attain our sample size indicates that 14 per cent of the time in NGC 2516 and 17 per cent of the time in NGC 2422 we would expect to see no G stars with elevated $v_r \sin(i)$ – i.e. above the visual envelope traced by the bulk of stars in the left panels of Figs 14 and 15 – assuming our data samples well the underlying distribution. The Pleiades sample

reported in Queloz et al. (1998) has no early to mid K stars with rotation rates above $\sim 20 \text{ km s}^{-1}$, at odds with our sample. Comparing our NGC 2516 and NGC 2422 samples, we find that they are in agreement except for early K stars, where we see many higher rotation stars in the NGC 2516, despite its older age. A Monte Carlo simulation suggests there is only a 9 per cent chance that their early K distributions are similar. Table 6 reports means and standard deviations for $v_r \sin(i)$ for three temperature ranges roughly corresponding to the F, G and K stars in our sample.

We combine our data for $v_r \sin(i)$, $[\text{Fe}/\text{H}]$, membership and binarity in Figs 16 and 11, which are colour–magnitude and temperature–magnitude diagrams for our clusters. As previously mentioned, the enhanced metallicity among members hotter than $\sim 6000 \text{ K}$ is likely an artefact of the stars’ higher stellar rotation and our fitting approach. The disagreement between G and K stars does not follow from this as our K star spectra appear not to suffer from the same optimization issue.

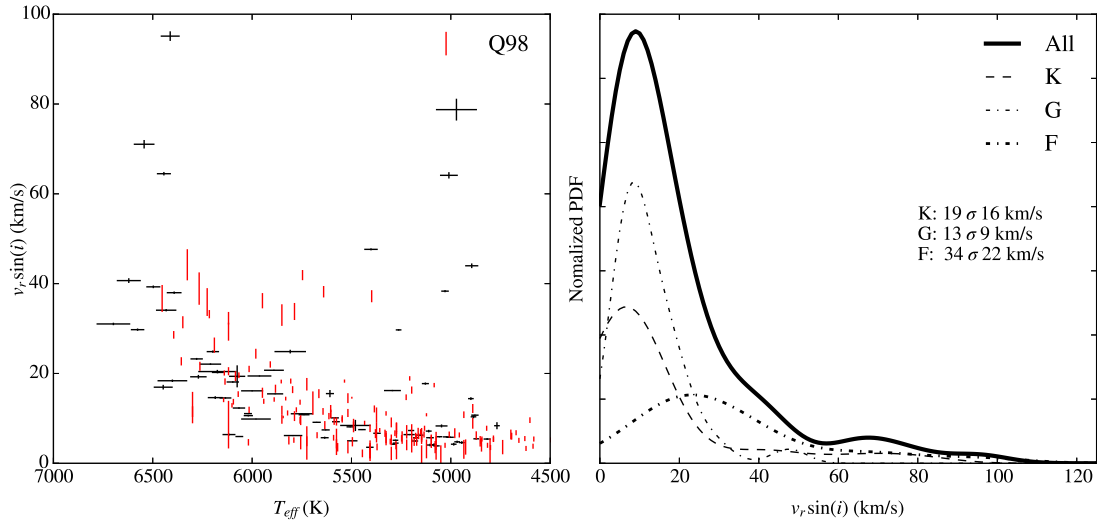


Figure 14. Left: $v_r \sin(i)$ values we measure for RV members in NGC 2516 as a function of corrected T_{eff} along with values for stars in the Pleiades taken from tables 3 and 4 of Queloz et al. (1998) in red. We have used Casagrande et al. (2010) with $[\text{Fe}/\text{H}] = +0.02$ and $E(B - V) = 0.04$ to convert colours to temperatures for Pleiades stars. Right: Gaussian kernel density estimates for the RV members grouped by spectral type.

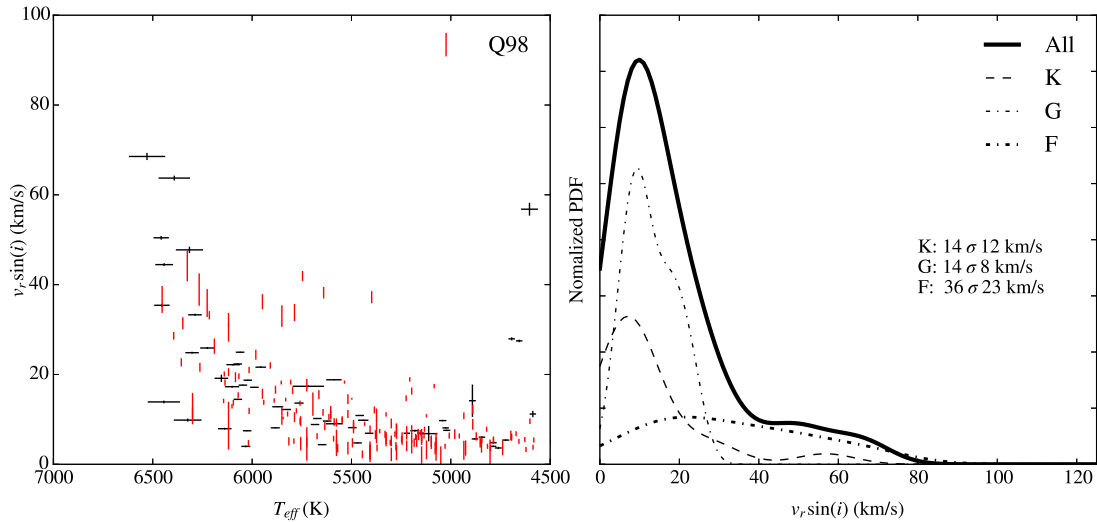


Figure 15. Left: $v_r \sin(i)$ values we measure for RV members in NGC 2422 as a function of corrected T_{eff} along with values for stars in the Pleiades taken from tables 3 and 4 of Queloz et al. (1998) in red. We have used Casagrande et al. (2010) with $[\text{Fe}/\text{H}] = +0.02$ and $E(B - V) = 0.04$ to convert colours to temperatures for Pleiades stars. Right: Gaussian kernel density estimates for the RV members grouped by spectral type.

Table 6. Aggregate $v_r \sin(i)$ values.

Cluster	$T_{\text{eff}} \geq 6100 \text{ K}$ (km s^{-1})	$5250 \text{ K} \leq T_{\text{eff}} < 6100 \text{ K}$ (km s^{-1})	$T_{\text{eff}} < 5250 \text{ K}$ (km s^{-1})
NGC 2516	33 ± 20.9 ($N = 20$)	13 ± 9.0 ($N = 24$)	14 ± 18.0 ($N = 33$)
NGC 2422	31 ± 16.2 ($N = 11$)	13 ± 5.6 ($N = 24$)	13 ± 12.8 ($N = 18$)
Non-members	31 ± 26.1 ($N = 25$)	5 ± 1.3 ($N = 44$)	5 ± 5.4 ($N = 44$)

Note. Means and standard deviations for $v_r \sin(i)$ measurements of RV members in each of our targeted clusters as well as an aggregate value for all RV non-members. Stars are grouped by measured T_{eff} .

7 STELLAR JITTER

Young stars are well known to exhibit stellar activity (e.g. surface spots and flares) that can induce measurable distortions in line profiles, thereby shifting the recovered RVs from their true values (for a review, see Lagrange et al. 2013). Stars as young as those

in the ~ 140 -Myr- and ~ 75 -Myr-old clusters we have targeted are often avoided in exoplanet searches for fear of stellar jitter hindering detection of low-amplitude RV variability. Levels in excess of 300 m s^{-1} are seen at ages of a few million years (see fig. 3 of Lagrange et al. 2013) in RVs obtained from optical spectra while others have reported values of 60 m s^{-1} at ~ 200 Myr (Paulson &

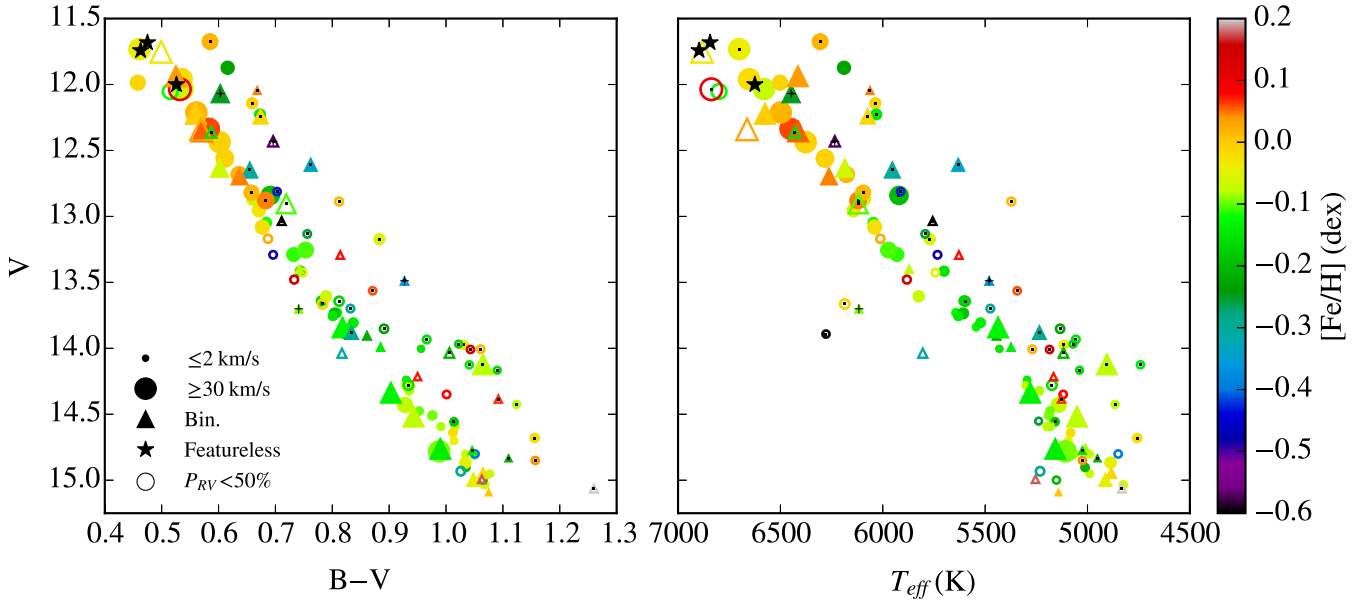


Figure 16. Colour–magnitude (left) and temperature–magnitude (right) diagrams for targets in NGC 2516. Stars we identified as probable members (see Section 5) are shown as filled circles or, for binaries, triangles. Double-lined binaries have a tiny black + on them and targets J01 identifies as photometric binaries a tiny black dot. The colour shows [Fe/H] and point size $v_r \sin(i)$. Unfilled points show the same for targets that do not pass our membership test. The filled black stars correspond to the featureless spectra discussed in Section 5.1 and are plotted using T_{B-V} . We have corrected the T_{eff} values of members using equation (2).

Yelda 2006). IR spectra can reduce activity-induced variations by about twofold due to the decreased star-spot contrast ($\sim 100 \text{ m s}^{-1}$ at 15 Myr; Bailey et al. 2012) but this approach is usually hindered by smaller wavelength coverage and noisier detectors.

Stars older than ~ 500 Myr show significantly reduced activity with levels below 20 m s^{-1} in the optical (Paulson et al. 2004; Quinn et al. 2012, 2014). To date, there is no generally accepted level of jitter as a function of age in the ~ 30 – 500 Myr range, though this may be because there is not one. The large spread in stellar rotation and activity exhibited by coeval stars with ages of ~ 50 – 300 Myr may well mean a one-size-fits-all approach is not applicable (Lagrange et al. 2013). In this section, we investigate the level of stellar jitter, σ_{jitter} , seen and, despite our comment regarding one-size-fits-all approaches, attempt to determine an average value for each cluster.

In Section 4, we introduced σ_{stel} to quantify the level of stellar velocity variability we see beyond that explained by our measurement errors alone. There we argued that any variability seen above a 300 m s^{-1} threshold was induced purely by the presence of a stellar companion, neglecting variations caused by stellar activity. As levels at these ages are likely $\lesssim 150 \text{ m s}^{-1}$ (Lagrange et al. 2013), that choice did not appreciably affect our binary determinations and allowed us to defer the detailed issue until now. We defined

$$\sigma_{\text{stel}} \equiv \sqrt{\sigma_{\text{obs}}^2 - \sigma_{\text{meas}}^2},$$

where σ_{obs}^2 is the measurement weighted variance in our RV measurements and σ_{meas}^2 is the mean measurement variance. Here we acknowledge the contribution of jitter explicitly with the approximation that $\sigma_{\text{stel}}^2 = \sigma_{\text{companion}}^2 + \sigma_{\text{jitter}}^2$ and point out that in the absence of a companion, σ_{stel} serves as a measure of σ_{jitter} .

Fig. 17 shows σ_{stel}^2 versus $v_r \sin(i)$ for the different subsets – RV members and non-members, RV binaries and RV variables – in a log–log plot. This plot shows clearly that many stars in our sample exhibit greater variability than one would expect from measurement errors alone. A higher proportion of non-member stars have

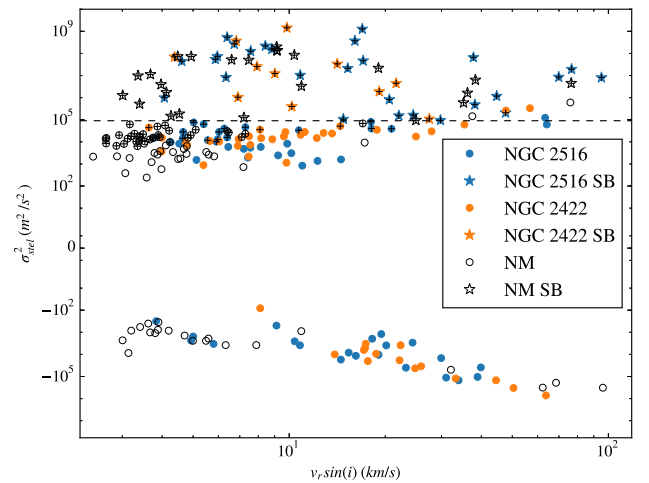


Figure 17. σ_{stel}^2 versus $v_r \sin(i)$ for stars in our sample. Circles denote RV single stars and stars denote RV binary stars. Unfilled markers are targets that failed our membership test. A black cross has been placed on markers that show statistically significant RV variability. Blue marks indicate members of NGC 2516 and orange of NGC 2422. The dashed horizontal line demarcates our RV binary threshold.

a comparable (or greater) σ_{meas} than σ_{obs} , as might be expected in a population composed of older field dwarfs and giants and hence subject to less stellar activity (e.g. Johnson et al. 2010). The frequency of stars with a negative σ_{stel}^2 and $v_r \sin(i) < 8 \text{ km s}^{-1}$ is consistent with our simulated data set. At higher rotation rates, we see more stars with a variance deficit, consistent with our mean RV prior biasing our results towards non-variability.

We employ two different approaches to estimate a typical value for σ_{jitter} in each cluster. The first is to ask what the mean level of stellar variability is in our sample ($\sqrt{\sigma_{\text{stel}}^2}$). The second and more

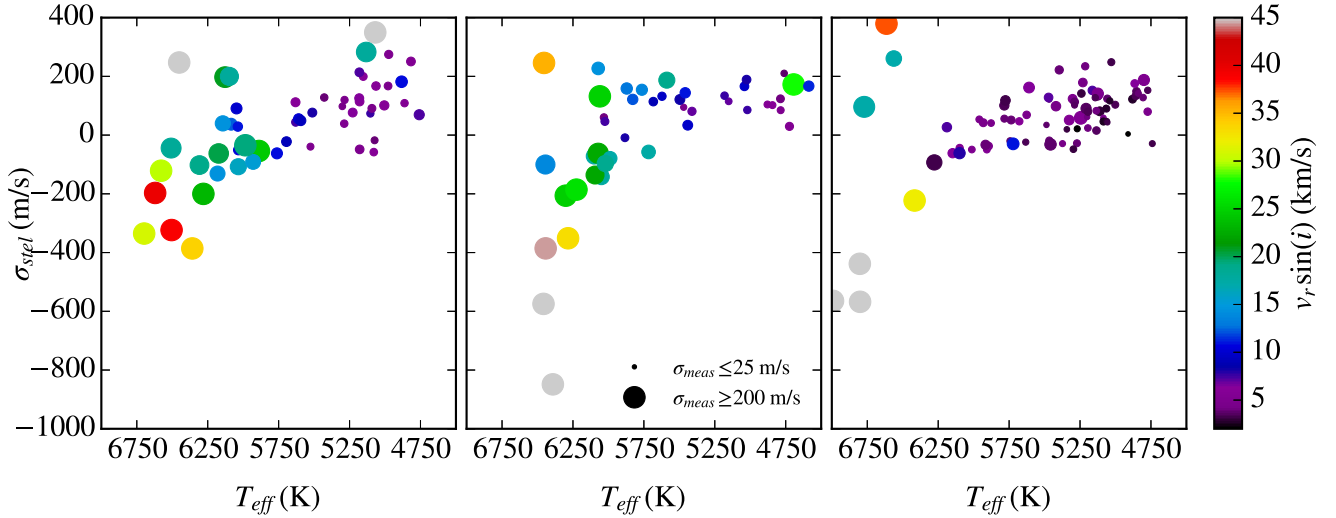


Figure 18. σ_{stel} as a function of T_{eff} for non-binaries in NGC 2516 (left), NGC 2422 (middle) and the combined sample of non-members (right). Point sizes are scaled by the mean measurement error for each target and point colour is used to show $v_r \sin(i)$. We plot negative values for σ_{stel} by computing the root of the absolute value of the variance and preserving the sign. The large number of rapidly rotating stars with negative σ_{stel} is a result of our optimizer exhibiting a strong preference for the initial RV in spectra with broad features. Based on this figure, we adopt the $T_{\text{eff}} < 5800$ K and $v_r \sin(i) < 15$ km s $^{-1}$ sample to study stellar activity in our sample.

Table 7. Stellar jitter.

Method	NGC 2516	σ_{jitter} (m s $^{-1}$) NGC 2422	Non-members
1	48 \pm 29 (14)	131 \pm 44 (18)	90 \pm 31 (45)
2	77 \pm 10 (18)	138 \pm 10 (19)	56 \pm 7 (30)
Averages	74 \pm 9	138 \pm 2	58 \pm 7

Note. Numbers in parentheses report sample size. An additional 10 m s $^{-1}$ has been added to correct for the underestimate seen in our simulations.

involved method is to assume that each star’s set of RV measurements is drawn from Gaussians at each star’s absolute RV with widths $\sigma^2 = \sigma_{\text{meas}}^2 + \sigma_{\text{stel}}^2$, then we determine the likelihood function for σ_{stel} given our data and solve for σ_{stel} with maximum likelihood. In both cases, we must consider the $\sigma_{\text{companion}}$ contribution of genuine companions; recall from Section 5.2 that we expect at least 37 per cent of stars with $\sigma_{\text{stel}} < 300$ m s $^{-1}$ to be long-period binaries. We account for companions in our sample in two ways. First, we compute the mean or expectation value of σ_{stel} iteratively, excluding any stars with a ≥ 99 per cent chance of being a variable ($P_v \geq 0.99$; Section 8) in the presence of the jitter inferred from the previous iteration. Secondly, we apply both tests to our simulated population (Section 4.1) in the presence of added Gaussian jitter. We find that each method recovers a jitter estimate ~ 10 m s $^{-1}$ under the input value and that the two methods agree at the m s $^{-1}$ level.

We use RV single members ($\sigma_{\text{stel}} < 300$ m s $^{-1}$) with a corrected $T_{\text{eff}} < 5800$ K and $v_r \sin(i) < 15$ km s $^{-1}$ (Fig. 18) in NGC 2516 ($N = 30$) and NGC 2422 ($N = 20$) to estimate the level of stellar activity in our targets. In practice, these temperature and rotation cuts are equivalent to a measurement error cut of $\sigma_{\text{meas}} < 100$ m s $^{-1}$, which we use when testing our approach with simulated data. The two tests we perform are described in the following paragraphs and the results are listed in Table 7. Fig. 19 shows the starting and final samples for method 2. The set of targets used is similar for the first method. Although we observe significant variability in our non-member sample, we argue that the poorer accuracy of the stellar templates used for these fits (i.e. very inaccurate log (g)

values and hence poorly optimized T_{eff} and [Fe/H]) may mean that we underestimate our measurement errors. We also note that the jitter we recover is about the same as our median value for σ_{meas} .

Method 1 We compute $\sqrt{\sigma_{\text{stel}}^2}$. This yields 122 ± 58 m s $^{-1}$ using 30 stars in NGC 2516, which converges to 38 ± 29 m s $^{-1}$ ($N = 14$) after iteratively excluding probable variables. In NGC 2422, we measure a value of 130 ± 50 m s $^{-1}$ using 20 stars, which converges to 121 ± 44 m s $^{-1}$ ($N = 18$) after iteratively excluding stars with $P_v \geq 0.99$. Our simulation suggests that these values systematically underestimate the true variability by 10 m s $^{-1}$.

Method 2 We assume that our RVs (x_{ij}) are drawn from a set of Gaussians each located at a star’s relative motion along the line of sight (μ_i) and a standard deviation corresponding to the quadrature sum of $\sigma_{\text{meas},i}$ and σ_{stel} :

$$(x_{11}, x_{1j}, \dots, x_{NM_i}) \sim N \left(\mu_i, \sqrt{\sigma_{\text{meas},i}^2 + \sigma_{\text{stel}}^2} \right).$$

The likelihood function for which is

$$f_{\sigma_{\text{stel}}, \mu_1, \dots, \mu_N}(\mathbf{X}_1, \dots, \mathbf{X}_N) = \prod_{i=1}^N \prod_{j=1}^{M_i} \frac{1}{\sqrt{2\pi(\sigma_{\text{meas},i}^2 + \sigma_{\text{stel}}^2)}} e^{-\frac{x_{ij} - \mu_i}{2(\sigma_{\text{meas},i}^2 + \sigma_{\text{stel}}^2)}}. \quad (4)$$

Noting that

$$\frac{1}{M_i} \sum_{j=1}^{M_i} (x_{ij} - \bar{x}_i)^2 \approx \sigma_{\text{obs},i}^2$$

and that $\mu_i \approx \bar{x}_i$, we can take the log and write the log-likelihood as

$$l(\sigma_{\text{stel}}) = -\frac{1}{2} \sum_{i=1}^N M_i \times \left(\frac{\sigma_{\text{obs},i}^2}{\sigma_{\text{meas},i}^2 + \sigma_{\text{stel}}^2} + \log \left(2\pi \left(\sigma_{\text{meas},i}^2 + \sigma_{\text{stel}}^2 \right) \right) \right). \quad (5)$$

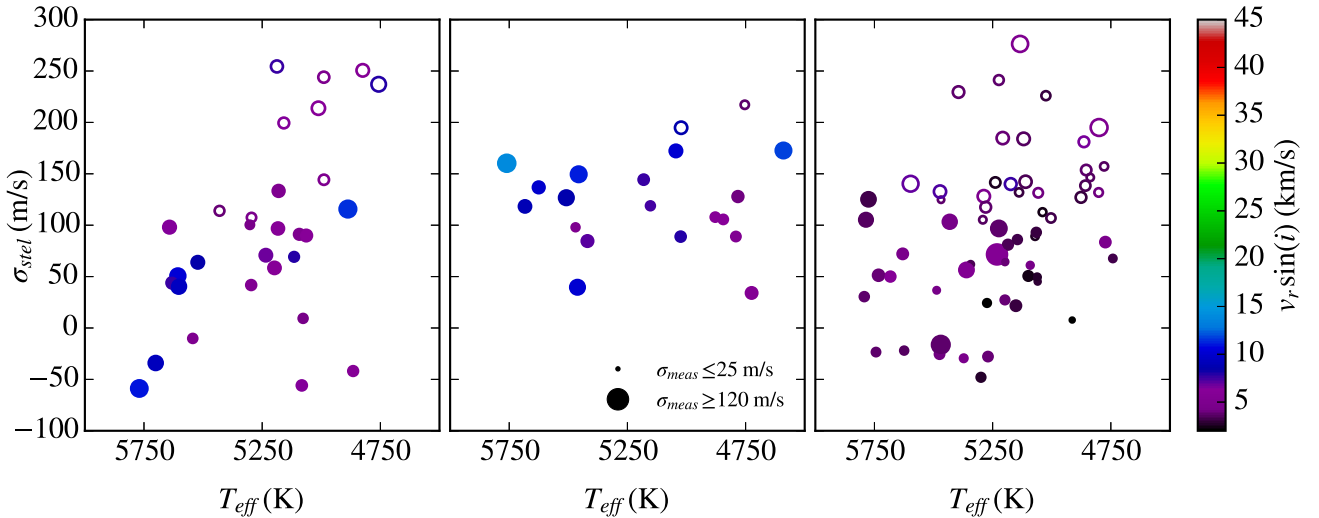


Figure 19. Starting and ending samples of σ_{stel} used to estimate stellar activity levels in NGC 2516 (left), NGC 2422 (middle) and the combined sample of non-members (right) with method 2 (method 1 is similar). Point sizes are scaled by the mean measurement error for each target and point colour is used to show $v_r \sin(i)$. Open circles denote targets that were excluded by the $P_v \geq 0.99$ cut when iterating. Negative values for σ_{stel} are the root of the absolute value of the variance with the sign preserved.

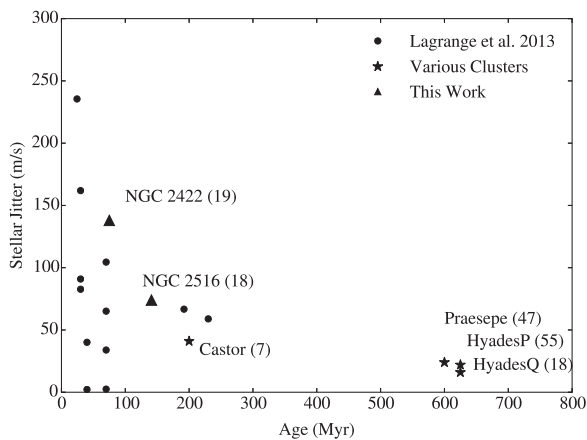


Figure 20. Determinations of stellar jitter for a number of single stars (circles) from Lagrange et al. (2013), averages from stars in open clusters and young associations from Paulson & Yelda (2006), Paulson et al. (2004) and Quinn et al. (2012, 2014) (stars), and our results in NGC 2516 and NGC 2422 (triangles). For clusters and associations, we note the name and number of stars used in the average.

Here N is the number of stars under consideration and M_i the number of observations of star i . The peak of this function then provides an estimate of typical σ_{stel} for the sample of stars, which after iterating should be predominately driven by companion-free (or effectively so) stars. We find $\sigma_{\text{stel}} = 130 \pm 10 \text{ m s}^{-1}$ using 30 stars in NGC 2516, which converges to $67 \pm 10 \text{ m s}^{-1}$ ($N = 18$) after iteratively excluding stars with $P_v > 0.99$. In NGC 2422, we measure a value of $135 \pm 10 \text{ m s}^{-1}$ using 20 stars, which converges to $128 \pm 10 \text{ m s}^{-1}$ ($N = 19$). Our simulation suggests that these values systematically underestimate the true variability by 10 m s^{-1} . Table 7 also reports values for the non-member population.

In Fig. 20, we show the levels of jitter we measure in NGC 2516 and NGC 2422 alongside measurements of stellar jitter in single stars from Lagrange et al. (2013, measured using HARPS at $\sim 530 \text{ nm}$) and the values determined by various other authors (also in the optical) for a number of open clusters and associations. Our

results in both clusters are generally consistent with existing results: large scatter when young, decreasing to $\lesssim 150 \text{ m s}^{-1}$ by $\sim 100 \text{ Myr}$. Note that our observed rotation rates in NGC 2422 (Table 6) are consistent with those in NGC 2516 but the binary fraction in NGC 2516 is far higher, suggesting that neither stellar rotation nor binarity are to blame for NGC 2422’s higher activity. In both clusters, and NGC 2516 especially, we measured a wide range of σ_{stel} in our non-variable population, suggesting there is, indeed, a large spread in activity-induced RV variability among individual stars as was previously seen at $\sim 50\text{--}75 \text{ Myr}$ in the work of Lagrange et al. (2013) and shown in Fig. 20.

8 STELLAR VARIABILITY

We now turn our attention to identifying which stars in our sample exhibit statistically significant RV variability and to placing limits on companion masses for our entire sample. Our goal here is to provide a refined pool of targets that merit following up with some combination of single-object RV spectroscopy and multi-band photometric monitoring to assess whether stellar surface activity is responsible for the variability we see.

We compute the raw probability that each star is an RV variable and the probability that each star is an RV variable in the presence of the appropriate σ_{jitter} from Table 7. This probability, $P_v = P(X < \chi^2)$, is computed using the RVs and σ_{meas} values of each star, in the latter case incorporating σ_{jitter} by adding in quadrature with σ_{meas} . In both cases, we exclude RV outliers $> 3\sigma_{\text{obs}}$ from the mean RV. This excludes a single epoch for 42 stars and two epochs in another two stars for a total of 44 RVs across our sample of ~ 2500 observations. The former raw P_v then is an estimate of the likelihood that each star exhibits any sort of velocity variability while the latter estimates the probability that variations are induced by a companion. These probabilities are reported in Tables A1 and A2.

We performed the same analysis on our simulated RVs to estimate the false-positive and false-negative rates for stellar and exoplanetary companions as a function of P_v cut and gauge our companion sensitivity. Figs 21 and 22 show our false-positive and false-negative

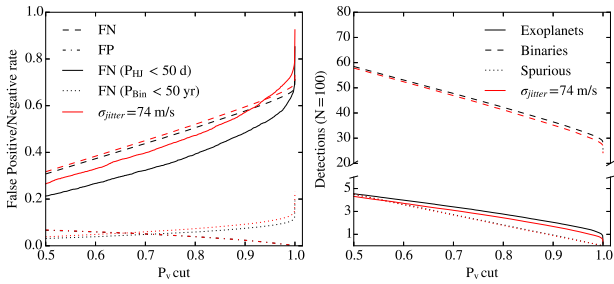


Figure 21. Left: False-positive (FP) and false-negative (FN) rates of our variability test for binaries and exoplanets in our companion simulation for NGC 2516 both without (black) and with (red, styles the same as for black lines) additional stellar variability. Right: The number of true binaries (not merely binaries with $\sigma_{\text{stel}} > 300 \text{ m s}^{-1}$), exoplanet-hosting and spuriously variable stars we would expect to flag in a sample of 100 stars, again shown without (black) and with (red) additional stellar variability. This simulation was run assuming a binary fraction of 85 per cent consistent with **J01** and assuming the cadence of our 12 observations in NGC 2516. Though not shown, we note a binary fraction of 100 per cent would increase the expected number of binary detections by approximately seven, roughly independent of P_v cut.

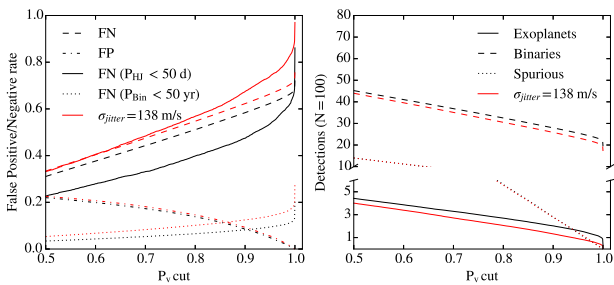


Figure 22. Left: False-positive (FP) and false-negative (FN) rates of our variability test for binaries and exoplanets in our companion simulation for NGC 2422 both without (black) and with (red, styles the same as for black lines) additional stellar variability. Right: The number of true binaries (not merely binaries with $\sigma_{\text{stel}} > 300 \text{ m s}^{-1}$), exoplanet-hosting and spuriously variable stars we would expect to flag in a sample of 100 stars, again shown without (black) and with (red) additional stellar variability. This simulation was run assuming a binary fraction of 62 per cent and assuming the cadence of our ten observations in NGC 2422.

rates as a function of P_v along with the number of exoplanets, binaries and false variables we would expect in a population of 100 stars for each of our clusters. This indicates that for a P_v cut of 0.96, we can expect a roughly equivalent number of exoplanet hosts as false positives while being sensitive to 92 per cent of binaries with $P \lesssim 50$ yr and ~ 40 per cent of simulated exoplanets with $P < 50$ d. Assuming NGC 2516 has a binary fraction of 85 per cent, consistent with **J01**, and a jitter of 74 m s^{-1} , our simulations predict RV binaries ($\sigma_{\text{stel}} > 300 \text{ m s}^{-1}$) to be composed of 99 per cent stellar multiples, 0.85 per cent exoplanets and 0.15 per cent false positives. Low-amplitude variables should be composed of 84 per cent stellar, 12 per cent exoplanets and 4 per cent false positives. In NGC 2422, we adopt a binary fraction of 62 per cent and predict binaries to be composed of 97.6 per cent stellar, 1.4 per cent exoplanets and 1 per cent false positives. Our single sample should consist of 67 per cent binaries, 12 per cent exoplanets and 21 per cent false positives.

Table 8. Number of RV variables stars in NGC 2516 and NGC 2422.

Group	NGC 2516 sample		NGC 2422 sample	
	Members	Non-members	Members	Non-members
Usable targets	81	41	57	65
RV variables	52	26	35	47
RV variables including σ_{jitter}	43	23	14	35
SB2	2/3 (2)	1/1 (1)	2/2	1/2
$\sigma_{\text{stel}} \geq 300 \text{ m s}^{-1}$	16/27 (10)	8/13 (7)	7/11	7/11
$\sigma_{\text{stel}} < 300 \text{ m s}^{-1}$	2/16 (4)	1/10 (8)	0/3	6/24

Note. This is a breakdown of RV variability in our sample. Usable targets exclude the five featureless stars, the one star in NGC 2516 for which no usable data were obtained and the one mistakenly targeted early-type star in NGC 2422 (Section 5.1). The first of each pair of numbers is the number of RV variables with at least a 95 per cent significant periodogram peak (Section 8.1). This number is followed by the total number of statistically significant ($P_v > 0.96$) RV variables, accounting for a jitter level of 74 m s^{-1} in NGC 2516, 138 m s^{-1} in NGC 2422 and 58 m s^{-1} in the field. Numbers in parentheses denote the number of stars in common with photometric binaries reported by **J01**. Sections 5 and 8 describe the expected make-up of these groups in terms of multiples, long-period multiples, exoplanets and false positives. Tables 9 and 10 provide details of the variables in NGC 2516 and NGC 2422.

8.1 RV variables

Adopting a P_v threshold of 0.96, we report the number of significant RV variables we see in Table 8 after accounting for the average σ_{jitter} from Table 7. 53 of our single stars exhibit significant variability after accounting for stellar jitter.

Using a binary fraction of 100 per cent in NGC 2516, $\sigma_{\text{jitter}} = 74 \text{ m s}^{-1}$, our observation spacing and our adopted threshold of $P_v = 0.96$, we would expect 39 per cent of members to exhibit significant variability. We observe a significantly higher total variability rate of 53 ± 6 per cent. Our simulation shows we would expect about 50 per cent for the total variability rate if the true value for σ_{jitter} were in agreement with NGC 2422. As we used only stars with $T_{\text{eff}} < 5800 \text{ K}$ and $v_r \sin(i) < 15 \text{ km s}^{-1}$ when computing σ_{jitter} , one possibility is that hotter or more rapidly rotating stars make up the majority of these variables. However, that is not the case. Only three of the 16 low-amplitude variables are hot enough or fast enough rotators to be affected by this cut; excluding them lowers our total variability to 49 per cent. Additional data (e.g. activity indicators) or targeted monitoring is needed to address the source of this disagreement.

In NGC 2422, with a binary fraction of 62 per cent and $\sigma_{\text{jitter}} = 138 \text{ m s}^{-1}$, we would expect 25 per cent of members to exhibit significant variability. We find a total variability rate of 25 ± 6 per cent, in good agreement with our expectations.

We used the **GATSPY** package (VanderPlas & Ivezić 2015) to compute Lomb–Scargle periodograms and estimate their significance via a bootstrap simulation for all of our RV variable stars. Of the 62 binaries, 38 exhibit periodogram peaks with >95 per cent significance and have periods ranging from just over a day (our data suffers from a strong alias below ~ 1.1 d) to ~ 3.5 yr. Nine RV single stars also exhibited significant peaks with seven between 1.5 and 5.8 d, one at 21 d and one at 27 d. We then used **SYSTEMIC2** (Meschiari et al. 2012) to fit trial orbits to each of these stars and perform MCMC simulations to estimate possible companion masses and refine the orbital period. Fig. 23 shows the refined periods as a function of σ_{obs} as well as the median $M \sin(i)$ against the refined periods. This draws into stark relief the larger than expected number of exoplanet

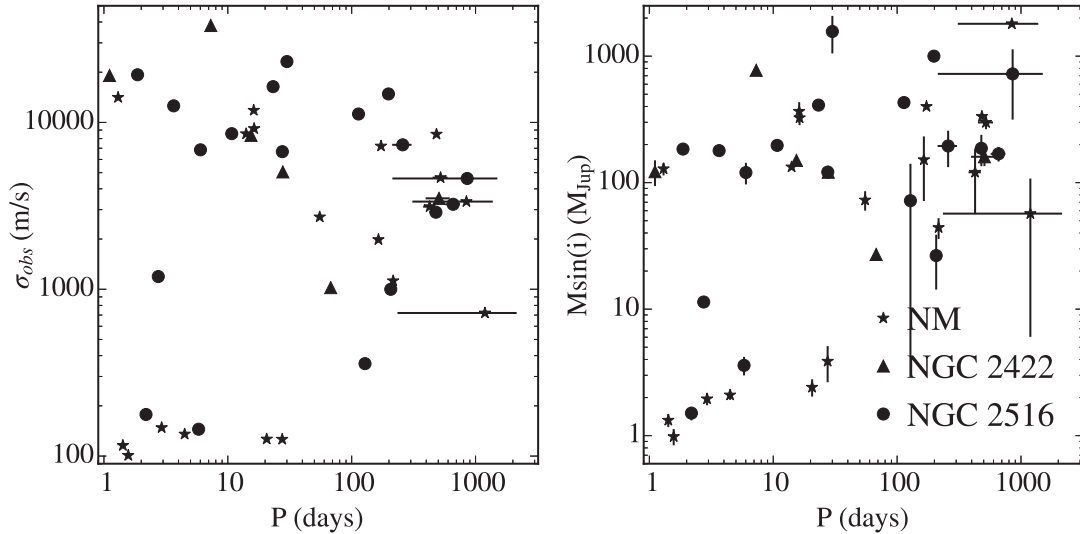


Figure 23. Left: Observed RV standard deviation versus median MCMC period. Right: Inferred companion $M \sin(i)$ versus period. Host star masses were computed using the mass–radius relation of Torres et al. (2010) along with our fitted T_{eff} (corrected for members by equation 2), $[\text{Fe}/\text{H}]$ and our adopted $\log(g)$. The masses may, therefore, be significantly off for any non-member giant stars in our sample.

host candidates in our sample, especially for non-member stars. Assuming 1.2 per cent of stars in our sample possess a hot Jupiter companion, we would predict a 1 in 4 chance of there being three in our sample of 81 (two real and one spurious per our false alarm predictions) and expect about a 1 in 10 chance of there being three with one false alarm in our field sample.

The figures in Appendix B (online only) show RV time series, periodograms and – for variables with a significant peak $\gtrsim 1.1$ d – phased RV curves. We stress that these periods should be considered speculative without follow-up observations. Points shown as a red X were excluded for being $>3\sigma$ outliers. References to these figures are provided in Tables 9 and 10. These are subsets of our full results table, which consists of key values for RV variables in NGC 2516 and NGC 2422. NGC 2516 has undergone extensive X-ray study and we use the captions of the individual plots to mention any known X-ray variability from D03 or Wolk et al. (2004). For comparison, we also show a selection of RV time series for six non-variable stars in Fig. 24, the properties of which are summarized in Table 11.

8.2 Short-period companion detection limits

We determined companion-mass detection limits via Monte Carlo simulations at representative orbital periods of 3, 10 and 20 d. The 3 d period is chosen to be near the peak in the orbital period distribution of hot Jupiters (Winn & Fabrycky 2015) while the other periods are chosen to demonstrate how the sensitivity declines with increasing orbital period, given the precision and temporal sampling of our survey. At each period, we used our companion detectability simulations (Section 4.1), including the appropriate mean σ_{jitter} (74 m s^{-1} in NGC 2516, 138 m s^{-1} in NGC 2422 and 58 m s^{-1} for non-members) to determine the fraction of orbits for which we would recover $P_v > 0.96$. We simulated 2500 orbits per Jupiter-mass interval over the region from approximately half detectable to 95 per cent detectable and then carried the simulation as far beyond; e.g. a star with ~ 50 per cent of companions detectable at $10 M_{\text{Jup}}$ and ~ 95 per cent detectable at $30 M_{\text{Jup}}$ would have 100 000 orbits simulated from 10 to $50 M_{\text{Jup}}$. This resulted in between 75 000 and 1.45 million orbits (mean 120 000) simulated for each star and-

measured the parameter space around the 95 per cent threshold was well sampled without requiring excessive simulation time. We then fitted each detected fraction with an incomplete gamma function and adopted the point at which our fit crossed the 95 per cent detectable threshold as our companion-mass limit. We used the mass–radius relation of Torres, Andersen & Giménez (2010) along with our adopted T_{eff} , $[\text{Fe}/\text{H}]$ and $\log(g)$ to determine a mass for the primary.

The resulting mass limits are reported in Tables A1 and A2. On average for non-variable RV members, we are able to exclude companions greater than 7.4 , 11.3 and $23 M_{\text{Jup}}$ in NGC 2516 and 9.5 , 14.4 and $26.1 M_{\text{Jup}}$ in NGC 2422 at periods of 3, 10 and 20 d. For RV non-members, we exclude companions at 7.3 , 11.2 and $21.4 M_{\text{Jup}}$ on average. These thresholds are heavily influenced by the subset of our sample, which has large measurement errors: the same measures using only stars with $\sigma_{\text{meas}} < 150 \text{ m s}^{-1}$ are ~ 50 per cent lower. Indeed, for approximately 1/3 of our non-variable stars, we can exclude 3 d companions more massive than $3 M_{\text{Jup}}$.

9 SUMMARY

We have presented the first results of our survey of Sun-like stars in the core 0.5° fields of NGC 2516 and NGC 2422. We constructed spectral models of approximately 2700 high-spectral-resolution ($R \sim 50\,000$) observations at $7165\text{--}7295 \text{ \AA}$ made with the M2FS on the Clay telescope at Las Campanas Observatory. We used telluric absorption features as an absolute, simultaneous wavelength reference. Each spectrum was modelled as the combination of a telluric spectrum and a synthetically generated stellar spectrum, convolved by a parametrized instrumental profile and projected on to a pixel-space grid.

We used our modelling approach (described fully in B16) to make determinations of RVs, T_{eff} , $[\text{Fe}/\text{H}]$, $[\alpha/\text{Fe}]$ and $v_r \sin(i)$ for nearly all 126 and 125 stars in our NGC 2516 and NGC 2422 samples along with estimates for total cluster binary fractions of 100^{+0}_{-15} per cent and 62 ± 16 per cent. Of the surveyed stars, 81 and 57 proved to be RV members, 12 of which were not previously identified by photometry in NGC 2422. We also noted the presence of a RV clustering of 11 stars along a line of sight to the Monoceros stream

Table 9. Variables in NGC 2516.

UCAC4	Flags	N	$\overline{S/N}$	T_{eff} (K)	$v_r \sin(i)$ (km s $^{-1}$)	RV (m s $^{-1}$)	σ_{obs} (m s $^{-1}$)	σ_{meas} (m s $^{-1}$)	σ_{stel} (m s $^{-1}$)	P_v	Period (days)	Figure
147-012265	PMSB2	11	115	6447 \pm 50	16.9 \pm 0.5	37677 \pm 11052	35789	196	35789	1.00	–	B1
147-012424	PMSB2	12	54	6116 $^{+35}_{-33}$	6.4 \pm 0.2	15450 \pm 6734	23160	75	23160	1.00	30.0	B2
146-012601	PMB	10	39	5239 \pm 19	16.1 \pm 0.2	31158 \pm 6325	19304	159	19303	1.00	1.9	B3
147-012249	MB	12	51	5372 $^{+17}_{-13}$	6.7 \pm 0.1	25997 \pm 4535	16386	62	16386	1.00	23.2	B4
147-012499	PMSB2	12	51	5480 \pm 79	8.4 \pm 1.3	18343 \pm 4125	14814	87	14814	1.00	78.7	B5
146-012500	PMB	11	27	5001 \pm 30	8.8 \pm 0.2	16724 \pm 4637	12569	267	12567	1.00	3.7	B6
146-012622	NMSB2	11	59	6234 \pm 207	9.2 \pm 0.3	– 1954 \pm 4049	11821	176	11819	1.00	16.2	B7
146-012455	PMB	12	45	5430 $^{+21}_{-18}$	7.6 \pm 0.1	28014 \pm 3450	11231	74	11231	1.00	113.5	B8
147-012487	NMB	12	85	6408 $^{+35}_{-28}$	10.4 $^{+0.2}_{-0.1}$	15591 \pm 2803	9182	105	9181	1.00	16.3	B9
148-012940	PMB	11	108	6063 $^{+22}_{-19}$	6.0 \pm 0.1	30821 \pm 2475	8563	47	8562	1.00	10.8	B10
146-012358	NMB	11	29	4833 \pm 18	4.5 \pm 0.2	69487 \pm 3072	8545	60	8545	1.00	14.1	B11
146-012557	NMB	12	74	5731 \pm 34	4.9 \pm 0.2	– 30760 \pm 2369	8502	68	8502	1.00	1283.6	B12
147-012308	MB	11	93	6403 $^{+49}_{-45}$	37.8 \pm 0.3	25169 \pm 2493	8136	399	8126	1.00	–	B13
147-012432	MB	11	39	5022 \pm 19	5.9 \pm 0.2	26179 \pm 2333	7340	60	7340	1.00	559.5	B14
147-012270	NMB	7	46	5117 \pm 60	7.5 \pm 0.6	16154 \pm 2929	7084	80	7084	1.00	34.3	B15
147-012164	MB	12	97	6070 \pm 46	17.0 \pm 1.9	23279 \pm 1930	6851	163	6849	1.00	6.0	B16
147-012262	MB	11	25	4945 \pm 19	4.6 \pm 0.3	23031 \pm 2187	6679	84	6678	1.00	27.6	B17
148-012906	MB	11	100	5631 $^{+22}_{-19}$	15.3 \pm 1.0	26429 \pm 1406	4613	115	4611	1.00	497.4	B18
147-012376	MB	5	25	5042 \pm 116	76.7 \pm 2.5	25225 \pm 2351	4591	1322	4397	1.00	–	B19
147-012474	NMB	12	37	5111 \pm 20	3.7 \pm 0.1	– 500 \pm 975	3353	43	3353	1.00	545.3	B20
147-012175	MB	12	26	4877 $^{+17}_{-13}$	10.8 \pm 0.2	23748 \pm 981	3231	108	3229	1.00	445.5	B21
148-012943	PMB	12	122	6412 \pm 48	95.1 \pm 1.1	22513 \pm 1032	3135	1326	2841	1.00	–	B22
147-012290	NMB	11	47	5160 $^{+18}_{-13}$	3.4 \pm 0.2	12026 \pm 942	3126	42	3125	1.00	987.3	B23
147-012280	MB	11	106	6553 \pm 79	69.9 \pm 0.9	25578 \pm 978	3111	1052	2928	1.00	–	B24
146-012365	MB	12	52	5864 $^{+21}_{-18}$	6.3 \pm 0.1	22849 \pm 882	2896	78	2895	1.00	492.3	B25
147-012220	NMB	12	91	6887 \pm 80	76.5 \pm 1.1	20925 \pm 807	2488	1306	2118	1.00	–	B26
147-012205	NMB	12	73	5631 $^{+21}_{-18}$	4.0 \pm 0.1	14106 \pm 625	1985	41	1984	1.00	52.0	B27
147-012406	NMB	11	92	6645 \pm 67	36.2 \pm 0.7	21242 \pm 414	1351	448	1275	1.00	–	B28
146-012483	MB	12	30	4899 \pm 48	44.7 \pm 0.5	22790 \pm 367	1191	498	1082	1.00	2.7	B29
147-012433	MB	11	25	5126 \pm 23	4.1 \pm 0.3	25744 \pm 321	999	64	997	1.00	82.0	B30
146-012424	MB	12	86	5934 \pm 50	20.6 \pm 0.1	25703 \pm 302	926	185	907	1.00	–	B31
147-012306	MB	11	37	5035 \pm 23	38.2 \pm 0.3	26249 \pm 264	793	382	694	1.00	–	B32
146-012520	MB	12	52	5401 \pm 50	47.7 \pm 0.3	24940 \pm 229	648	460	455	0.99	–	B33
147-012251	MB	11	69	6182 $^{+36}_{-29}$	24.5 \pm 0.2	24331 \pm 195	519	326	404	1.00	–	B34
147-012272	MB	11	76	6249 \pm 47	22.1 \pm 0.2	24747 \pm 152	454	230	392	1.00	–	B35
147-012231	NMB	8	25	5250 $^{+26}_{-22}$	4.5 \pm 0.4	15581 \pm 149	435	59	431	1.00	–	B36
146-012416	NMB	11	70	6118 \pm 44	25.0 \pm 0.2	27520 \pm 127	398	251	309	1.00	–	B37
146-012534	MB	12	45	5264 \pm 19	29.8 \pm 0.2	24480 \pm 132	396	249	308	1.00	–	B38
146-012369	NMB	11	33	5791 \pm 64	7.2 \pm 0.8	5191 \pm 130	379	138	352	1.00	–	B39
146-012602	MB	11	24	4900 $^{+18}_{-15}$	14.8 \pm 0.2	23787 \pm 115	358	147	327	1.00	95.0	B40
146-012421	M	11	27	5133 \pm 25	18.0 \pm 0.2	26057 \pm 112	336	181	283	1.00	–	B41
146-012444	M	11	28	4974 $^{+18}_{-13}$	5.0 \pm 0.2	25696 \pm 95	282	65	275	1.00	–	B42
147-012463	M	12	68	6127 $^{+35}_{-30}$	20.9 $^{+0.2}_{-0.1}$	24565 \pm 98	276	192	197	0.98	–	B43
147-012166	M	12	27	4817 \pm 18	5.4 \pm 0.2	24584 \pm 72	260	70	251	1.00	–	B44
147-012503	M	12	61	6097 $^{+35}_{-27}$	18.1 \pm 0.2	24371 \pm 91	260	166	200	0.99	–	B45
147-012380	NM	11	29	5030 $^{+18}_{-14}$	3.2 \pm 0.2	2714 \pm 78	254	53	248	1.00	–	B46
147-012407	M	11	39	5181 $^{+18}_{-13}$	7.3 \pm 0.2	22685 \pm 69	225	70	214	1.00	–	B47
147-012446	M	11	44	5154 $^{+18}_{-16}$	6.3 \pm 0.2	23504 \pm 68	208	61	199	1.00	–	B48

Table 9 –continued

UCAC4	Flags	N	$\overline{S/N}$	T_{eff} (K)	$v_r \sin(i)$ (km s ⁻¹)	RV (m s ⁻¹)	σ_{obs} (m s ⁻¹)	σ_{meas} (m s ⁻¹)	σ_{stel} (m s ⁻¹)	P_v	Period (days)	Figure
147-012375	M	12	30	4883 ± 25	10.7 ± 0.2	25355 ± 61	207	99	182	1.00	–	B49
146-012368	NM	12	39	5609 ± 25	6.5 ± 0.2	22379 ± 56	186	91	162	1.00	–	B50
147-012307	M	11	30	5064 ⁺¹⁸ ₋₁₄	6.0 ± 0.2	24607 ± 60	180	67	167	1.00	–	B51
146-012532	M	11	30	4979 ⁺¹⁸ ₋₁₄	4.7 ± 0.2	24935 ± 57	178	60	167	1.00	2.2	B52
147-012156	NM	6	17	5125 ⁺²⁴ ₋₁₉	4.9 ± 0.5	17041 ± 80	170	95	141	0.99	–	B53
147-012460	NM	12	40	5163 ⁺¹⁷ ₋₁₅	7.3 ± 0.1	22417 ± 54	166	68	152	1.00	–	B54
147-012428	NM	12	34	5240 ± 18	2.9 ± 0.2	74928 ± 49	153	58	142	1.00	–	B55
146-012330	M	9	28	5182 ⁺²⁰ ₋₁₅	6.4 ± 0.2	24284 ± 51	145	72	125	1.00	5.8	B56
146-012470	M	11	38	5429 ⁺²² ₋₁₉	3.9 ± 0.1	23245 ± 47	140	57	128	1.00	–	B57
146-012487	NM	10	37	5058 ⁺¹⁹ ₋₁₄	3.7 ± 0.3	– 1191 ± 44	136	55	124	1.00	–	B58
146-012374	M	12	46	5631 ± 25	6.0 ± 0.1	23340 ± 40	133	72	112	0.99	–	B59
147-012349	M	11	39	5285 ⁺¹⁸ ₋₁₃	4.6 ± 0.2	25375 ± 39	132	55	120	1.00	–	B60
146-012681	M	10	39	5005 ± 20	5.9 ± 0.2	24628 ± 43	126	75	101	0.97	–	B61
147-012400	NM	12	46	5040 ⁺¹⁷ ₋₁₃	2.7 ± 0.1	97180 ± 36	125	45	116	1.00	–	B62
146-012635	M	11	39	4862 ⁺¹⁸ ₋₁₃	5.6 ± 0.2	22942 ± 37	122	56	109	1.00	–	B63
146-012496	NM	5	22	5111 ± 33	2.9 ± 0.6	20 ± 50	108	71	81	1.00	–	B64
147-012199	NM	12	59	5067 ⁺¹⁷ ₋₁₃	2.7 ± 0.1	89852 ± 30	101	42	92	1.00	1.6	B65
146-012372	NM	11	39	5194 ⁺¹⁸ ₋₁₆	3.3 ± 0.2	77675 ± 34	97	56	80	0.98	–	B66

Note. RV Variables in the NGC 2516 field. The period is given for stars having more than six epochs and a peak (aside from the alias seen at ~1 d) exceeding 95 per cent significance. Derived values used our mean jitter level of 74 m s⁻¹ for members and 58 m s⁻¹ for non-members. Figure references are for Appendix B, which is available online.

Table 10. Variables in NGC 2422.

UCAC4	Flags	N	$\overline{S/N}$	T_{eff} (K)	$v_r \sin(i)$ (km s ⁻¹)	RV (m s ⁻¹)	σ_{obs} (m s ⁻¹)	σ_{meas} (m s ⁻¹)	σ_{stel} (m s ⁻¹)	P_v	Period (days)	Figure
378-036252	PMSB2	10	156	6324 ± 73	9.8 ± 0.3	47929 ± 12207	38107	95	38107	1.00	7.3	B67
377-035049	MSB2	10	24	5112 ± 47	6.8 ± 1.7	37337 ± 7180	19124	117	19124	1.00	10.1	B68
378-036176	NMSB2	10	122	6102 ± 148	9.1 ± 1.2	4337 ± 4762	14124	110	14123	1.00	1.3	B69
379-035886	NMSB2	7	16	4999 ± 44	9.2 ± 4.4	26035 ± 3938	11504	190	11502	1.00	–	B70
379-035649	PMB	10	60	5648 ⁺²³ ₋₂₁	4.4 ± 0.1	38661 ± 2646	8366	41	8366	1.00	15.4	B71
379-036197	NMB	10	110	6299 ⁺³⁸ ₋₃₀	6.6 ± 0.2	11379 ± 2426	7216	59	7215	1.00	160.8	B72
379-035982	MB	8	45	4890 ⁺²¹ ₋₁₆	14.1 ± 3.5	36530 ± 2159	5799	120	5798	1.00	2.0	B73
378-036328	MB	10	116	6138 ⁺³⁸ ₋₃₀	7.9 ± 0.2	36928 ± 1520	5051	69	5050	1.00	27.7	B74
379-035884	NMB	10	124	6846 ⁺⁵² ₋₄₀	19.0 ± 0.3	59672 ± 1476	4667	235	4661	1.00	559.4	B75
378-036136	MB	10	27	5586 ± 41	9.0 ± 0.2	35631 ± 1181	3506	108	3505	1.00	543.7	B76
377-034854	NMB	10	94	6543 ± 105	38.3 ± 1.0	24943 ± 932	2713	1020	2514	1.00	55.2	B77
379-036066	PMB	8	88	5957 ± 28	21.6 ± 0.2	38029 ± 778	2125	198	2116	1.00	–	B78
378-036422	NMB	10	67	5310 ± 23	10.9 ± 0.2	43789 ± 633	1821	82	1819	1.00	59.8	B79
379-036005	PMB	10	86	6155 ⁺³⁸ ₋₃₀	19.1 ± 0.8	38391 ± 426	1386	207	1371	1.00	–	B80
379-036194	NMB	9	28	5425 ± 29	4.1 ± 0.2	106551 ± 465	1314	66	1312	1.00	–	B81
378-036137	NMB	10	81	5503 ± 24	3.0 ± 0.2	119993 ± 361	1123	49	1122	1.00	230.3	B82
378-036814	MB	10	49	5221 ⁺¹⁹ ₋₁₅	6.9 ± 0.2	36322 ± 335	1023	68	1021	1.00	67.9	B83
377-035019	NMB	10	48	4555 ⁺¹⁹ ₋₁₄	35.2 ± 0.6	32857 ± 261	805	238	769	1.00	–	B84
378-036277	NMB	10	61	5382 ⁺²³ ₋₂₀	3.4 ± 0.1	27815 ± 229	721	38	720	1.00	1286.7	B85
378-036531	MB	10	73	5672 ⁺²³ ₋₂₀	10.2 ± 0.1	37361 ± 199	635	78	630	1.00	–	B86
379-035545	NMB	10	23	4980 ⁺¹⁹ ₋₁₄	4.3 ± 0.2	115336 ± 141	389	64	384	1.00	–	B87
379-035711	MB	10	38	4656 ⁺¹⁹ ₋₁₄	27.5 ± 0.3	35190 ± 131	378	184	330	1.00	–	B88
377-034937	NM	10	75	6563 ⁺³⁸ ₋₃₀	17.0 ± 0.2	18602 ± 103	296	139	261	1.00	–	B89

Table 10 – *continued*

UCAC4	Flags	N	$\overline{S/N}$	T_{eff} (K)	$v_r \sin(i)$ (km s $^{-1}$)	RV (m s $^{-1}$)	σ_{obs} (m s $^{-1}$)	σ_{meas} (m s $^{-1}$)	σ_{stel} (m s $^{-1}$)	P_v	Period (days)	Figure
377-035026	M	10	92	6072 $^{+23}_{-20}$	14.5 \pm 0.1	36139 \pm 82	252	110	227	0.99	–	B90
377-034926	NM	10	34	5214 \pm 24	4.1 \pm 0.2	98342 \pm 77	241	55	234	1.00	–	B91
378-036663	NM	9	32	5397 \pm 27	3.9 \pm 0.3	79984 \pm 86	231	65	222	1.00	–	B92
378-036905	M	9	31	4761 $^{+20}_{-15}$	3.6 \pm 0.3	35560 \pm 75	215	47	210	0.99	–	B93
378-036547	NM	9	17	4800 \pm 21	5.1 \pm 0.6	19528 \pm 75	210	94	188	1.00	–	B94
378-036894	M	10	36	5026 $^{+19}_{-17}$	8.1 \pm 0.2	36279 \pm 66	201	69	189	0.98	–	B95
377-034990	NM	10	25	5230 \pm 40	4.2 \pm 0.2	105039 \pm 58	192	69	179	1.00	–	B96
378-036447	NM	10	36	4864 $^{+19}_{-14}$	6.4 \pm 0.2	38416 \pm 66	186	60	176	1.00	–	B97
378-036274	NM	10	21	4852 $^{+19}_{-17}$	3.5 \pm 0.3	14484 \pm 58	160	59	149	1.00	–	B98
377-034927	NM	10	37	4773 $^{+19}_{-14}$	3.3 \pm 0.2	6905 \pm 52	159	46	153	1.00	–	B99
377-035048	NM	6	33	5125 $^{+24}_{-21}$	3.2 \pm 0.4	45989 \pm 65	150	68	134	1.00	–	B100
379-035798	NM	10	38	4839 $^{+19}_{-14}$	3.9 \pm 0.2	102809 \pm 44	148	42	142	1.00	2.9	B101
378-036680	NM	10	51	5472 $^{+23}_{-20}$	7.1 \pm 0.1	10075 \pm 53	145	69	128	1.00	–	B102
378-036662	NM	9	22	4857 $^{+20}_{-15}$	3.4 \pm 0.2	119830 \pm 52	145	57	133	1.00	–	B103
379-036032	NM	7	16	5776 \pm 54	3.1 \pm 0.5	8763 \pm 64	142	79	118	0.98	4.1	B104
378-036665	NM	10	28	5303 \pm 29	4.8 \pm 0.2	109015 \pm 47	142	70	124	1.00	–	B105
378-036349	NM	10	38	4806 $^{+19}_{-14}$	3.9 \pm 0.2	–3348 \pm 51	137	48	128	1.00	–	B106
377-034915	NM	9	29	4880 $^{+20}_{-17}$	2.7 \pm 0.3	18566 \pm 51	136	60	122	1.00	–	B107
378-036777	NM	9	28	5143 $^{+20}_{-15}$	3.4 \pm 0.2	72053 \pm 44	135	46	127	1.00	4.5	B108
378-037002	NM	9	23	5288 $^{+25}_{-22}$	3.7 \pm 0.3	106495 \pm 45	128	60	113	1.00	–	B109
378-036376	NM	10	42	5468 $^{+23}_{-20}$	3.7 \pm 0.2	51164 \pm 43	126	37	121	1.00	20.5	B110
378-036080	NM	10	59	5784 \pm 28	3.3 \pm 0.2	20198 \pm 48	126	76	101	0.96	27.5	B111
378-036806	NM	9	27	5420 \pm 27	4.2 \pm 0.4	102882 \pm 47	125	77	98	0.96	–	B112
378-036256	NM	10	31	5002 $^{+19}_{-17}$	3.4 \pm 0.3	31331 \pm 41	116	52	103	1.00	1.4	B113
378-036312	NM	10	41	5289 $^{+23}_{-20}$	3.5 \pm 0.2	53252 \pm 37	110	42	102	1.00	–	B114
379-035569	NM	10	35	5064 $^{+19}_{-14}$	3.0 \pm 0.4	–23236 \pm 36	103	50	90	0.98	–	B115

Note. RV variables in the NGC 2422 field. The period is given for stars having more than six epochs and a peak (aside from the alias seen at ~ 1 d) exceeding 95 per cent significance. Derived values used our mean jitter level of 138 m s $^{-1}$ for members and 58 m s $^{-1}$ for non-members. Figure references are for Appendix B, which is available online.

among the RV non-member non-variable stars in our NGC 2422 sample (Section 5.4).

We identified 52 stellar or brown dwarf RV binaries ($\sigma_{\text{stel}} \geq 300$ m s $^{-1}$; see Section 4), 45 of which (17 in NGC 2516, 11 in NGC 2422 and 17 non-members) had not previously been identified as binaries. We were able to identify tentative periods for 38 of the RV binaries. The values are given in Tables 9 and 10. These periods suggest eight have lower mass limits consistent with brown dwarfs. We also reported the discovery of eight SB2s. Our sample of binaries is 99 per cent complete for $P \lesssim 8$ yr.

We found an average stellar-activity-induced RV uncertainty of 74 m s $^{-1}$ in NGC 2516 and 138 m s $^{-1}$ in NGC 2422, broadly consistent with the known values for stellar jitter at ages of 141 and 73 Myr, respectively (Fig. 20). After accounting for this uncertainty, we identified 43 statistically significant low-amplitude RV variables (16 in NGC 2516, 3 in NGC 2422 and 34 non-members). Nine (two in NGC 2516, one in NGC 2422 and six non-members) of these low-amplitude RV variables exhibited at least 95 per cent significant Lomb–Scargle periodogram peaks, all but one of which were consistent with a possible planetary companion. For RV non-variable stars in our sample, we are able to exclude companions more

massive than about 8, 12 and 24 M_{Jup} – on average – with 95 per cent confidence for orbits of 3, 10 and 20 d.

ACKNOWLEDGEMENTS

The authors gratefully acknowledge valuable discussions with Sam Quinn, Justin Cantrell, Colin Slater and Ian Roederer. JB acknowledges the support of the Netherlands Research School for Astronomy and the European Space Agency under European Space Research and Technology Centre contract 21114/07/NL/HBX. JB and MM acknowledge support from the National Science Foundation (NSF) astronomy and astrophysics research grant (AAG) 1312997 and the NSF/Major Research Instrumentation development grant 0923160. RW acknowledges support from NSF AAG 1517762. PyRAF is a product of the Space Telescope Science Institute, which is operated by the Association of Universities for Research in Astronomy for NASA. This research made use of ASTROPY, a community-developed core Python package for astronomy (Paunzen 2008). This research used the WEBDA database, operated at the Department of Theoretical Physics and Astrophysics of Masaryk University.

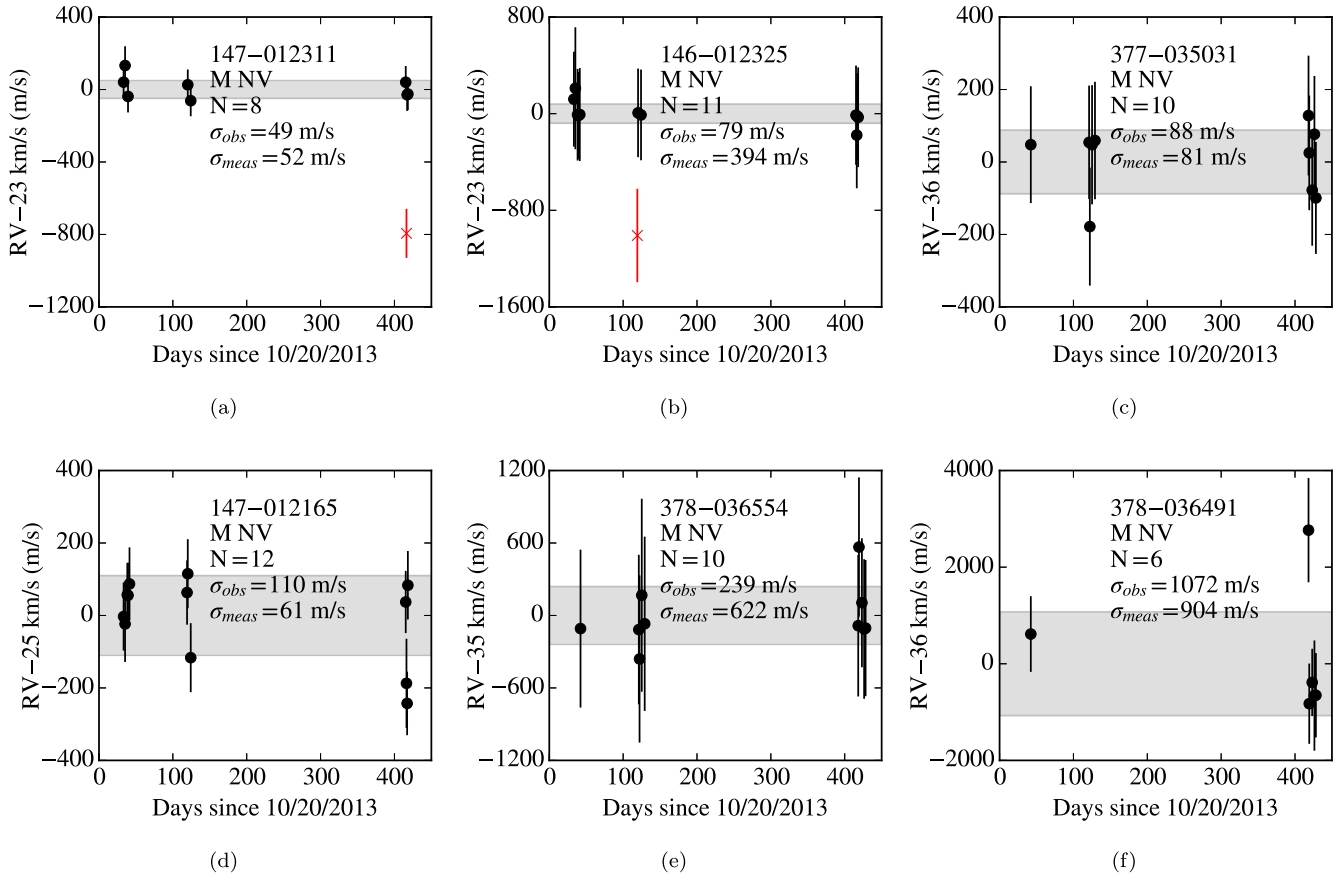


Figure 24. RV time series for a selection of RV non-variable stars in our sample. Properties are provided in Table 11. IDs starting with 1 are in NGC 2516 and 3 in NGC 2422. The grey band is of width $2\sigma_{\text{obs}}$. Red X's are epochs excluded as $>3\sigma_{\text{obs}}$ outliers. Membership and variability codes are shown for each star directly beneath the ID and are as described in the text. Errors shown include the appropriate σ_{jitter} .

Table 11. Selected RV non-variables in NGC 2516 and NGC 2422.

ID	N	S/N	T_{eff} (K)	$v_r \sin(i)$ (km s $^{-1}$)	RV (m s $^{-1}$)	σ_{obs} (m s $^{-1}$)	σ_{meas} (m s $^{-1}$)	P_v	Code	Plot
147-012311	8	31	5073^{+21}_{-16}	3.8 ± 0.2	22877 ± 25	49	52	0.11	M NV	Fig. 24a
146-012325	11	73	6359^{+49}_{-45}	33.9 ± 0.3	23481 ± 118	79	394	0.00	M NV	Fig. 24b
377-035031	10	63	5441 ± 26	9.8 ± 0.1	35610 ± 38	88	81	0.04	M NV	Fig. 24c
147-012165	12	31	5093^{+17}_{-13}	4.5 ± 0.2	25188 ± 38	110	61	0.86	M NV	Fig. 24d
378-036554	10	110	6458^{+52}_{-26}	50.4 ± 0.4	35165 ± 209	239	622	0.00	M NV	Fig. 24e
378-036491	6	17	4604 ± 44	56.8 ± 1.4	36151 ± 541	1072	904	0.90	M NV	Fig. 24f

Note. Properties for a selection of RV non-variable members stars in our sample. RV time series plots are shown in Fig. 24. IDs starting with 1 are in NGC 2516 and 3 in NGC 2422.

REFERENCES

Bailey John I., III, White R. J., Blake C. H., Charbonneau D., Barman T. S., Tanner A. M., Torres G., 2012, *ApJ*, 749, 16
 Bailey J. I., III, Mateo M., White R. J., Shectman S. A., Crane J. D., Olszewski E. W., 2016, *AJ*, 152, 9 (B16)
 Boss A. P., 1997, *Science*, 276, 1836
 Brucalassi A. et al., 2014, *A&A*, 561, L9
 Butler R. P., Marcy G. W., Williams E., McCarthy C., Dosanji P., Vogt S. S., 1996, *PASP*, 108, 500
 Casagrande L., Ramírez I., Meléndez J., Bessell M., Asplund M., 2010, *A&A*, 512, 54
 Damiani F., Flaccomio E., Micela G., Sciortino S., Harnden F. R., Jr, Murray S. S., Wolk S. J., Jeffries R. D., 2003, *ApJ*, 588, 1009 (D03)

Duchêne G., Kraus A., 2013, *ARA&A*, 51, 269 (DK13)
 Fabrycky D., Tremaine S., 2007, *ApJ*, 669, 1298
 Goldreich P., Tremaine S., 1980, *ApJ*, 241, 425
 Herbig G. H., Soderblom D. R., 1982, *ApJ*, 252, 610
 Howell S. B. et al., 2014, *PASP*, 126, 398
 Husser T. O., Wende-von Berg S., Dreizler S., Homeier D., Reiners A., Barman T., Hauschildt P. H., 2013, *A&A*, 553, A6
 Jeffries R. D., Thurston M. R., Hambly N. C., 2001, *A&A*, 375, 863 (J01)
 Johnson J. A., Howard A. W., Bowler B. P., Henry G. W., Marcy G. W., Wright J. T., Fischer D. A., Isaacson H., 2010, *PASP*, 122, 701
 Jurić M., Tremaine S., 2008, *ApJ*, 686, 603
 Kharchenko N. V., Piskunov A. E., Rösner S., Schilbach E., Scholz R. D., 2005, *A&A*, 438, 1163

- Lagrange A.-M., Meunier N., Chauvin G., Sterzik M., Galland F., Lo Curto G., Rameau J., Sosnowska D., 2013, *A&A*, 559, A83
- Lin D. N. C., Bodenheimer P., Richardson D. C., 1996, *Nature*, 380, 606
- Loktin A. V., Gerasimenko T. P., Malysheva L. K., 2001, *Astronom. Astrophys. Trans.*, 20, 607
- Mateo M., Bailey J. I., Crane J., Sheckman S., Thompson I., Roederer I., Bigelow B., Gunnels S., 2012, *Proc. SPIE*, 8446, 84464Y
- Meibom S. et al., 2013, *Nature*, 499, 55
- Meschiari S., Wolf A. S., Rivera E., Laughlin G., Vogt S., Butler P., 2012, *Astrophysics Source Code Library*, ascl:1210.018
- Meynet G., Mermilliod J.-C., Maeder A., 1993, *A&AS*, 98, 477
- Mizuno H., 1980, *Prog. Theor. Phys.*, 64, 544
- Nissen P. E., 1988, *A&A*, 199, 146
- Paulson D. B., Yelda S., 2006, *PASP*, 118, 706
- Paulson D. B., Cochran W. D., Hatzes A. P., 2004, *AJ*, 127, 3579
- Paunzen E., 2008, *CoSkS*, 38, 435
- Pillitteri I., Micela G., Damiani F., Sciortino S., 2006, *A&A*, 450, 993
- Prisinzano L., Micela G., Sciortino S., Favata F., 2003, *A&A*, 404, 927 (P03)
- Queloz D., Allain S., Mermilliod J.-C., Bouvier J., Mayor M., 1998, *A&A*, 335, 183
- Quinn S. N. et al., 2012, *ApJ*, 756, L33
- Quinn S. N. et al., 2014, *ApJ*, 787, 27
- Rasio F. A., Ford E. B., 1996, *Science*, 274, 954
- Robin A. C., Reylé C., Derrière S., Picaud S., 2003, *A&A*, 409, 523
- Schlafly E. F., Finkbeiner D. P., 2011, *ApJ*, 737, 103
- Slater C. T. et al., 2014, *ApJ*, 791, 9
- Soubiran C., Jasniewicz G., Chemin L., Crifo F., Udry S., Hestroffer D., Katz D., 2013, *A&A*, 552, A64
- Sung H., Bessell M. S., Lee B.-W., Lee S.-G., 2002, *AJ*, 123, 290
- Terndrup D. M., Pinsonneault M., Jeffries R. D., Ford A., Stauffer J. R., Sills A., 2002, *ApJ*, 576, 950
- Torres G., Andersen J., Giménez A., 2010, *A&AR*, 18, 67
- Udry S., Santos N. C., 2007, *ARA&A*, 45, 397
- van Dokkum P. G., 2001, *PASP*, 113, 1420
- VanderPlas J. T., Ivezić Ž., 2015, *ApJ*, 812, 18
- Walker M. G., Olszewski E. W., Mateo M., 2015, *MNRAS*, 448, 2717
- Wallace L., Hinkle K. H., Livingston W. C., Davis S. P., 2011, *ApJS*, 195, 6
- Winn J. N., Fabrycky D. C., 2015, *ARA&A*, 53, 409
- Wolk S. J. et al., 2004, *ApJ*, 606, 466
- Wright J. T., Marcy G. W., Howard A. W., Johnson J. A., Morton T. D., Fischer D. A., 2012, *ApJ*, 753, 160
- Zacharias N., Finch C. T., Girard T. M., Henden A., Bartlett J. L., Monet D. G., Zacharias M. I., 2013, *AJ*, 145, 44

SUPPORTING INFORMATION

Supplementary data are available at [MNRAS](https://academic.oup.com/mnras/article-abstract/475/2/1609/4820734) online.

Please note: Oxford University Press is not responsible for the content or functionality of any supporting materials supplied by the authors. Any queries (other than missing material) should be directed to the corresponding author for the article.

This paper has been typeset from a $\text{\TeX}/\text{\LaTeX}$ file prepared by the author.